On the Distribution of Convective and Stratiform Precipitation in Tropical Cyclones from Airborne Doppler Radar and Its Relationship to Intensity Change and Environmental Wind Shear Direction

JOSHUA B. WADLER,[a] JOSEPH J. CIONE,[b] ROBERT F. ROGERS,[b] AND MICHAEL S. FISCHER[b,c]

[a] Department of Applied Aviation Sciences, Embry-Riddle Aeronautical University, Daytona Beach, Florida
[b] NOAA/Atlantic Oceanographic and Meteorological Laboratory/Hurricane Research Division, Miami, Florida
[c] Cooperative Institute for Marine and Atmospheric Studies, University of Miami, Miami, Florida

ABSTRACT: Airborne Doppler radar reflectivity data collected in hurricanes on the NOAA P-3 aircraft between 1997 and 2021 were parsed into different modes of precipitation: stratiform precipitation, shallow convection, moderate convection, and deep convection. Stratiform precipitation was the most frequent precipitation mode with 82.6% of all observed precipitation while deep convection was the most infrequent at 1.3%. When stratified by 12-h intensity change, intensifying TCs had a greater areal coverage of total convection in the eyewall compared to weakening and steady-state TCs. The largest difference in the azimuthal distributions in the precipitation modes was in deep convection, which was mostly confined to the downshear-left quadrant in weakening and steady-state hurricanes and more symmetrically distributed in intensifying hurricanes. For all intensity change categories, the most symmetrically distributed precipitation mode was stratiform rain. To build upon the results of a recent thermodynamic study, the precipitation data were recategorized for hurricanes experiencing deep-layer wind shear with either a northerly component or southerly component. Like intensifying storms, hurricanes that experienced northerly component shear had a more symmetric distribution of deep convection than southerly component shear storms, which had a distribution of deep convection that resembled weakening storms. The greatest difference in the precipitation distributions between the shear direction groups were in major hurricanes experiencing moderate (4.5–11 m s^{-1}) wind shear values. Consistent with previous airborne radar studies, the results suggest that considering the distribution of deep convection and the thermodynamic distributions associated with differing environmental wind shear direction could aid TC intensity forecasts.

SIGNIFICANCE STATEMENT: This research investigates how the distribution of different types of precipitation are related to tropical cyclone (TC) intensity change. Even though deep convection—the tallest clouds—is the least frequent type of precipitation, it has the strongest relationship to intensity change with uniform distributions around the eyewall associated with intensification. Less significant relationships were noticed for shallower clouds and stratiform (lighter) rain. The study also analyzed how change in direction of the large-scale winds with height (wind shear) influences intensity change. When wind shear is northerly, there is a more symmetric distribution of deep convection compared to when wind shear is southerly. These relationships illustrate how wind shear direction influences TC convective structure and, in turn, TC intensity change.

1. Introduction

With the devastating loss of life and billions of dollars of property damage associated with tropical cyclone (TC) landfall (e.g., Pielke and Landsea 1998; Pielke et al. 2008; Klotzbach et al. 2018), the ability to produce accurate and timely forecasts of a storm's track and intensity remains critically important. Over recent years, track forecasts have improved more quickly than intensity forecasts, likely because of the complex multiscale interactions that control TC intensity change (e.g., Marks and Shay 1998; Rogers et al. 2006, 2013a; DeMaria et al. 2014; Cangialosi et al. 2020; Zawislak et al. 2022).

One of the primary drivers of TC intensity change is deep-layer environmental wind shear, often defined as the difference in area-averaged environmental winds between 850 and 200 mb (1 mb = 1 hPa). Jones (1995) used dry barotropic simulations to show that wind shear can lead to a tilted vortex which creates potential temperature anomalies that lead to isentropic ascent in the right-of-tilt direction and descent in the left-of-tilt direction. In real TCs, the shear-driven ascent tends to make the precipitation maximum preferentially occur in the downshear-left (DSL) quadrant and convective initiation in the eyewall preferentially occur in the downshear-right (DSR) quadrant (Black et al. 2002; Reasor et al. 2013; DeHart et al. 2014), which is also a region characterized by low-level convergence of vorticity and high equivalent potential temperature (θ_e) values (Riemer 2016). A tilted vortex can also allow for import of dry environmental air into the TC circulation (e.g., Davis and Ahijevych 2012; Zawislak et al. 2016; Nguyen et al. 2017; X. Chen et al. 2019; Fischer et al. 2023). Dry air can travel radially inward and directly mix with inner core convection (a process referred to as

Corresponding author: Joshua B. Wadler, wadlerj@erau.edu

radial ventilation; Tang and Emanuel 2010, 2012; Alland et al. 2017, 2021b), or can enter the inflow layer through downdrafts (a process referred to as downdraft ventilation; Riemer et al. 2010, 2013; Alland et al. 2021a) halting eyewall convective development if it is not recovered by air–sea enthalpy fluxes (Molinari et al. 2013; Zhang et al. 2013, 2017; Wadler et al. 2018a, 2021a; Nguyen et al. 2019; Rudzin et al. 2020; Chen et al. 2021).

The kinematic response of a TC to wind shear has been the focus of many recent observational and modeling studies. For example, many observational (e.g., Stevenson et al. 2014, 2018; Zagrodnik and Jiang 2014; Alvey et al. 2015; Rogers et al. 2013b, 2015, 2016; Rios-Berrios and Torn 2017; Wadler et al. 2018b; Fischer et al. 2018) and modeling studies (e.g., Chen and Gopalakrishnan 2015; Onderlinde and Nolan 2014, 2016; Rios-Berrios et al. 2016a,b; Leighton et al. 2018; Zhang and Rogers 2019) have shown that when deep convection is present in the eyewall of the upshear quadrants, there is a greater likelihood for subsequent intensification than when deep convection is confined to the downshear quadrants. These results support idealized modeling results which show that the projection of latent heating onto the wavenumber zero structure is important for TC intensification (e.g., Nolan and Grasso 2003; Nolan et al. 2007).

The vertical distribution of latent heating determines profiles of divergence, vertical mass flux, and terms in the vorticity budget (e.g., Bell and Montgomery 2019; Rogers et al. 2020; Nam and Bell 2021). Since these parameters depend on the mode of the precipitation (i.e., shallow, moderate, and deep convection, and stratiform precipitation), the amount of these various precipitation modes and their radial and azimuthal distributions can be correlated with TC intensity change. For example, a number of satellite studies have further linked the relative distribution of stratiform and moderate convective precipitation to subsequent TC intensity changes (e.g., Jiang 2012; Kieper and Jiang 2012; Zagrodnik and Jiang 2014; Alvey et al. 2015; Tao and Jiang 2015; Tao et al. 2017; Jiang et al. 2018; Pei and Jiang 2018). Using a 16-yr climatology from the Tropical Rainfall Measuring Mission (TRMM) satellite, Tao et al. (2017) showed that there is an increase in stratiform precipitation, particularly in the upshear-left (USL) quadrant, about 12 h before the onset of rapid intensification [RI; greater than or equal to a 30-kt intensity change over 24 h (1 kt $\approx$ 0.51 m s^{-1})]. Further stratifying by convective mode (i.e., shallow, moderate, or deep convection), Jiang et al. (2018) showed that there is an increase in shallow convection in the inner core ~3 h before RI. While the aforementioned satellite studies generally contrast with airborne radar composite studies, which have highlighted deep convection, often referred to as convective bursts, (e.g., Rogers et al. 2013b; Wadler et al. 2018b) as an indicator of RI, the differences could be attributed to differences in database size, differences in temporal continuity between the airborne and satellite-based platforms, and differences in spatial coverage between measurement platforms. Therefore, the relative importance of deep convection versus shallow/moderate convection and stratiform precipitation in TC intensification remains an open question. To date, no composite study has been conducted using airborne radar data, which can link precipitation mode

distributions to TC kinematic structures (e.g., vertical velocity), to relate the distribution of convective and stratiform precipitation to TC intensification.

In addition to a TC's response to vertical shear, recent work has also analyzed the relationship between TC intensity change to other properties of the environmental flow. For example, TC intensification has been linked to the depth of the wind shear (Finocchio et al. 2016), the direction of the low-level mean flow relative to the shear vector (e.g., Rappin and Nolan 2012; B.-F. Chen et al. 2018, 2019), and the sign of tropical cyclone relative environmental helicity (TCREH; Onderlinde and Nolan 2014, 2016; Gu et al. 2019). Additionally, the direction of the wind shear vector has been linked to TC genesis (Tuleya and Kurihara 1981; Nolan and McGauley 2012) and boundary layer thermodynamic distributions in developed storms (Cione et al. 2013). A recent composite study by Wadler et al. (2022) used the Tropical Cyclone Buoy Database (TCBD; Cione et al. 2000, 2013; Cione and Uhlhorn 2003) and dropsonde composites to show that the deep-layer wind shear direction is related to boundary layer thermodynamic distributions and TC intensity change. For all TCs subject to wind shear, there is a wavenumber-1 distribution in boundary layer thermodynamics with low-θ_e air due to downdrafts tending to occur in the primary rainband in the left-of-shear quadrants (e.g., Riemer et al. 2010). When wind shear has a southerly component, the downdraft-induced low-θ_e air is in phase with the background environmental θ_e gradient. This leads to the left-of-shear quadrants having statistically significant lower θ_e values throughout the boundary layer by 4–6 K than the right-of-shear quadrants. For convection to form within the eyewall of the DSR quadrant, this unfavorable asymmetric thermodynamic distribution requires significantly higher air–sea enthalpy fluxes downwind of the downdraft region as compared to when TCs experience shear with a northerly component, which tend to have more symmetric boundary layer distributions because the downdraft-induced low θ_e values are out of phase with the background environmental θ_e gradient. How the local thermodynamic environment for northerly component and southerly component shear cases translate to observed TC precipitation structure, and the impact of those precipitation structures on TC intensity change, is currently unknown and is the subject of this investigation.

The objectives of this study are to:

1) Use a composite radar database to characterize the distribution of precipitation modes in relation to TC intensity change; and
2) Compare the distribution of precipitation modes and its relationship to TC intensity change with the direction of the environmental wind shear vector and background thermodynamic distributions.

The study here is organized as follows: section 2 provides a description of the airborne radar database and the precipitation partitioning algorithm. Section 3 discusses precipitation distributions for different intensity change categories and horizontal directions of the environmental wind shear. Section 4

discusses the results and presents a discussion on how the precipitation distributions can relate to synoptic patterns, thermodynamic distributions, and TC intensity change. Section 5 provides the key takeaways and conclusions.

2. Data and methodology

a. P-3 tail-Doppler radar data

The primary data source used in this study to analyze the TC precipitation structure are pseudo dual-Doppler X-band tail-Doppler radar (hereafter TDR) analyses. TDR observations are routinely collected on the NOAA WP-3D (P-3) aircraft as part of the NOAA Intensity Forecasting Experiment (IFEX; Rogers et al. 2006, 2013a), which has recently transitioned to the Advancing the Prediction of Hurricanes Experiment (APHEX; Zawislak et al. 2022). This study utilizes the Tropical Cyclone Radar Archive of Doppler Analyses with Recentering (TC-RADAR) database version v3j (Fischer et al. 2022), which is comprised of over 1000 analyses from 306 flights into 74 TCs in the North Atlantic, eastern North Pacific, and central North Pacific basins between 1997 and 2021.

Each radar analysis is derived using a variational algorithm that solves the Doppler projection and continuity equations (Gamache 1997). Gridded-analyses are generated with a 2.0-km horizontal resolution and a 0.5-km vertical resolution (Reasor et al. 2009). Standard flight patterns include a rotated figure-4, figure-4, or butterfly, each including multiple radial inbound/outbound legs (descriptions of flight patterns are at https://www.aoml.noaa.gov/hurricane-field-program/) which provides a greater azimuthal data coverage during each mission, especially outside the inner-core.

Radar analyses are typically created for each radial penetration (inbound/outbound from the center) and a downwind leg, providing a swath of data within approximately 50 km of the flight track (Fischer et al. 2022). TDR swath analyses from the P-3 are commonly used to analyze convective and mesoscale processes within a TC (e.g., Rogers et al. 2015, 2016, 2020; Wadler et al. 2018a, 2021b; Fischer et al. 2020) and for composite characteristics of TC structure (e.g., Rogers et al. 2012, 2013b; Reasor et al. 2013; DeHart et al. 2014; Wadler et al. 2018b; Fischer et al. 2022). For each analysis, the TC center is identified as the analysis grid point that best matches a symmetric vortex of purely cyclonic flow. To summarize the center-finding process [see Fischer et al. (2022) for more details], the storm-relative wind direction at each grid point is compared to a flow that is purely tangential about a hypothetical TC center. This process is repeated for a series of hypothetical TC center locations. The TC center is identified as the analysis grid point that yields the lowest mean difference between the observed wind direction and the idealized cyclonic vortex, where the differences are weighted as functions of radius from the hypothetical TC center and the observed wind speed at each point. For each P-3 mission, TDR swath analyses are averaged together to create a merged analysis which is useful for diagnosing vortex-scale characteristics but can smear convective-scale characteristics where multiple swaths

overlap (e.g., Reasor et al. 2013). In this study, the merged analyses are only used for calculating the radius of maximum wind speed (RMW) which is uniformly referenced at 2-km altitude throughout this manuscript.

In addition to the TDR data, which contain three-dimensional wind speed, wind direction, and reflectivity, each swath and merged TDR analysis is linked to the nearest synoptic time to obtain vortex and environmental data from the Statistical Hurricane Intensity Prediction Scheme (SHIPS; DeMaria et al. 2005) database. This includes the TC intensity from the NHC best track data and the environmental wind shear vector, calculated by subtracting the 200–800-km radius area-averaged u and v components of the wind at 200 mb from those at 850 mb from the operational Global Forecasting System (GFS) analyses (variables SHTD and SHRD are used for shear direction and magnitude from the SHIPS database, respectively).[1] The database also contains the sea surface temperature (SST) which is calculated by linear interpolation of the weekly $1° \times 1°$ latitude–longitude Reynolds (Reynolds and Marsico 1993) SST obtained from the last available analysis prior to storm arrival.

Following Reasor et al. (2013), we restrict the database to TCs of hurricane intensity or greater to further ensure that the sampled TCs have well-defined circulations and sufficient radar coverage to compare azimuthal distributions of precipitation. Additionally, to lessen potential influences of land interactions on a storm's structure and intensity, swaths are eliminated for hurricanes that make landfall within 12 h after the completion of a P-3 mission. The resulting database contains 571 swaths from 175 missions for 52 hurricanes. The distribution of initial intensities from these swaths (Fig. 1a) shows a fairly equal sampling distribution across 65–120-kt intensity bins (from category 1 to middle category 4 on the Saffir–Simpson scale). Though less frequent, there are also swaths with initial intensities of 125 kt or greater (middle category 4 and category 5). The majority (44.3%) of hurricanes in the database experienced a subsequent 12-h intensity change classified as steady-state (SS; <10-kt intensity difference in 12 h) (Fig. 1b), while 33.3% of hurricanes underwent subsequent intensification (INT; ≥10 kt of intensity change in 12 h) and 22.4% underwent subsequent weakening (WE; ≤−10 kt of intensity change in 12 h). Note that the INT, SS, and WE definitions are consistent throughout the remainder of the analysis and that while this study uses 12-h intensity change criteria, similar results were obtained when INT and WE hurricanes were defined using an increase or decrease of 15 kt of intensity change over a 24-h period, respectively (not shown). Additionally, it is worth noting that the intensity change

---

[1] Because previous studies have found the direction and magnitude of vertical wind shear can vary depending on the spatial domain used to compute the shear (e.g., Reasor and Eastin 2012; Reasor et al. 2013; Boehm and Bell 2021; Dai et al. 2021; Ryglicki et al. 2021; Shi and Chen 2021), it is important to note that the shear-relative interpretations of the present study could vary if a smaller spatial domain was used to compute the shear. Future work should/will explore how the TC precipitation structure and intensity change is related to the spatial domain used to compute the vertical wind shear.
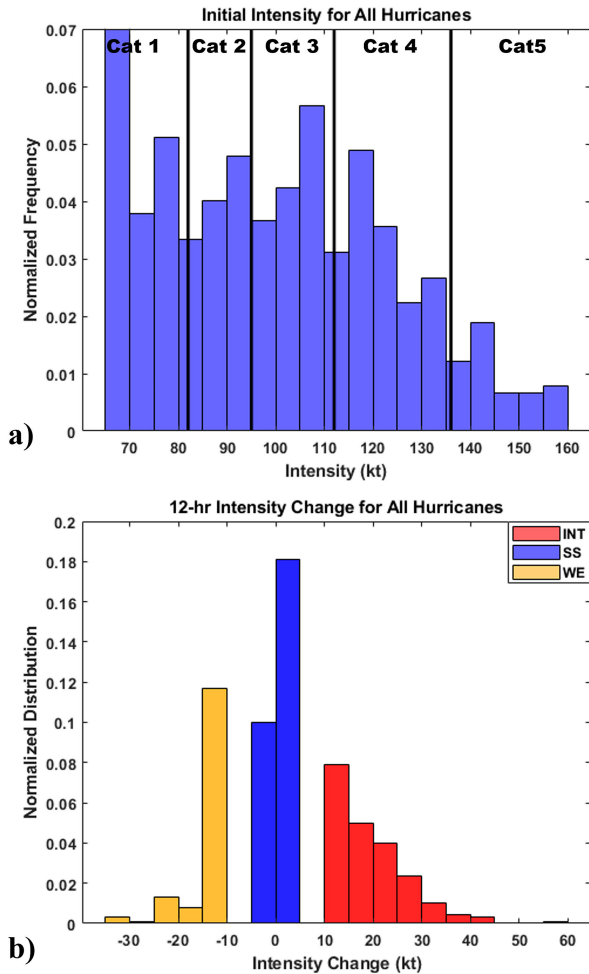
FIG. 1. Normalized frequencies of (a) initial hurricane intensities and (b) 12-h intensity change for all hurricanes in the P-3 tail Doppler radar database. In (a), hurricane categories on the Saffir–Simpson scale are outlined, and in (b), intensity changes cutoffs that qualify storms as undergoing subsequent weakening (WE), maintaining steady-state intensity (SS), and undergoing subsequent intensification (INT) are colored. Note that the gap in (b) is due to the intensities being reported in 5-kt increments.

criteria does not account for the intensity change prior to the analysis period. For example, a TC categorized as INT could have already been intensifying prior to the analysis time. Although satellite-based studies such as Tao and Jiang (2015) and Tao et al. (2017) have larger databases which can separate storms starting intensification with those undergoing continuous intensification, in the present study the sample sizes in the TC-RADAR database become too small for significance tests when further stratifying beyond the rate of intensity change.

b. Precipitation partition

A focal point of this study is the partition of TDR reflectivities into different precipitation modes (shallow/moderate/deep convection, stratiform precipitation, and weak echo). An initial concern with performing quantitative analyses using

radar reflectivity is that the radar systems on the two P-3s are not calibrated to each other, nor from season-to-season, which can lead to biases over time and differences between aircraft observing the same TC. To overcome this concern, a bias-correction technique was applied to cases in the TC-RADAR database (see the appendix). While this is not a complete calibration, the standardization of the reflectivity data between aircraft over many years minimizes the probability of ill-calibrated data influencing the results and facilitates a quantitative analysis of the full TC-RADAR database.

For every swath, the precipitation partitioning was performed using the original cartesian coordinates of the TDR analysis. The precipitation partition utilizes a three-step algorithm first discussed in Churchill and Houze (1984) and was applied by Steiner et al. (1995) for ground-based radar data. The algorithm has been further applied to airborne and ground-based radar data in studies by Didlake and Houze (2009), Rogers et al. (2020), Alvey et al. (2022), and Stone et al. (2023) and is similar to that used in the satellite-based study by Tao and Jiang (2015). First, the algorithm identifies a grid point as weak echo if the reflectivity at 2-km altitude is below 15 dBZ. Second, the algorithm identifies a grid point as convection if the reflectivity at a 2-km altitude grid point exceeds the critical threshold of 35 dBZ. A grid point can also be identified as convective if the reflectivity at the location exceeds the convective center criterion (ΔZ_{cc}) which is a function of area average background reflectivity in a disc with an 11-km radius (Z_{bg}) and tuning coefficients a and b [Eq. (1); Yuter and Houze 1997]:

$$\Delta Z_{cc} = a \cos\left(\frac{1}{b}\frac{\pi Z_{bg}}{2}\right). \tag{1}$$

In Didlake and Houze (2009) the tuning coefficients for Eq. (1) were $a = 9$ and $b = 25$ for the ELDORA airborne radar. The coefficients were verified to produce realistic precipitation partitions for P-3 TDR data in Rogers et al. (2020) and the present study through a subjective analysis of cross sections (an example is Fig. 2, which is discussed below). Last, since convection is seldom the size of a single grid point, a convective radius (R) is utilized [Eq. (2)], which is also a function of Z_{bg}, to determine if adjacent grid cells to previously determined convection can also be deemed convective:

$$R = \begin{cases} 0.5 & Z_{bg} < 20 \\ 0.5 + 3.5\left(\dfrac{Z_{bg} - 20}{15}\right) & 20 \le Z_{bg} < 35 \\ 4 & Z_{bg} \ge 35 \end{cases}. \tag{2}$$

All grid points not deemed convection or weak echo by the above criteria are designated as stratiform precipitation. Following the methodology in Rogers et al. (2020), for all convective grid points the convective depth was determined by the altitude of the 20-dBZ echo top [similar to the airborne radar studies by Rogers et al. (2013b), Wadler et al. (2018b)] and consistent with satellite-based studies of precipitation modes
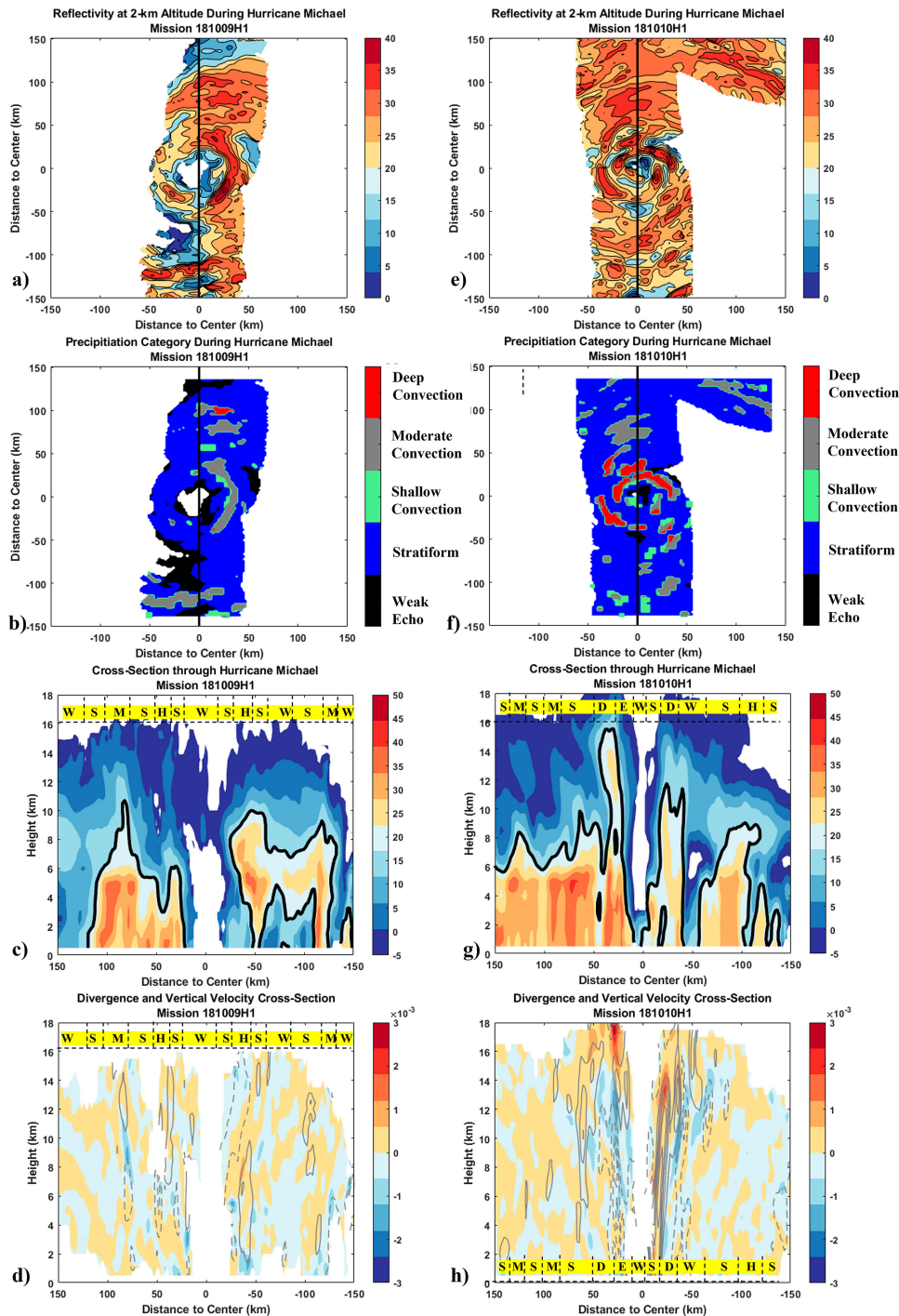
FIG. 2. (a) Radar reflectivity at 2-km altitude from a north–south pass during the 181009H1 mission (first P-3 mission on 9 Oct 2018 on *NOAA42*), and (b) objective precipitation partition of the reflectivity data during the mission in (a). The vertical line in (a) and (b) is to show where the cross section in (c) and (d) is taken from. (c) The cross section is north to south. The radar reflectivity is shaded and the 20-dB*Z* contour, which is used to determine the convective mode, is bolded. (d) The corresponding divergence (shaded) and vertical velocity (gray contour; positive is solid contour starting a 1 m s^{-1} at 1 m s^{-1} intervals, negative is dashed contour -1 m s^{-1} at 1 m s^{-1} intervals). Approximate outlines of the precipitation identified in (b) are given at the top of (c) and (d) with D = deep convection, M = moderate convection, H = shallow convection, S = stratiform precipitation, and W = weak echo. (e)–(h) As in (a)–(d), but for the 181010H1 mission (first P-3 mission on 10 Oct 2018 on *NOAA42*).

in TCs (e.g., Tao and Jiang 2015). A convective cell is deemed shallow, moderate, or deep if the 20-dBZ echo top is below 6 km (inclusive), between 6 and 10 km (inclusive of 10 km), or above 10 km, respectively. While the frequency of each convective mode is sensitive to the choice of the reflectivity threshold for separating the convection classifications, the value of 20 dBZ used here was found to produce realistic precipitation classifications from subjectively analyzing the algorithm applied to multiple TCs.[2]

An initial concern with applying a column-based partitioning algorithm to TCs of hurricane strength is potential misclassification of grid points due to tangential advection and outward eyewall slope. This is evaluated using an example of the classification algorithm for two time periods of Hurricane Michael (2018) in Fig. 2. Two missions from the same storm were chosen to demonstrate the evolution of the precipitation fields as the storm intensified from 90 (Figs. 2a–c) to 125 kt (Figs. 2d–f). A plan view during the first sampling period (Fig. 2b) shows shallow and moderate convection on the eastern side of the eyewall. The western side of the eyewall is mostly stratiform precipitation. A north–south cross section (Fig. 2c) shows a mix of shallow and moderate convection on the north side of the storm, with weaker convection and more stratiform rain on the south side. By the later sampling period, deep convection had developed around the northern side of the eyewall with some additional deep convection banding on the south side of the eyewall (Fig. 2e). The cross section shows the deep convection mostly within the innermost 50 km, accompanied with upper-level (>12-km altitude) divergence greater than 2×10^{-3} s^{-1} and vertical velocities greater than 2 m s^{-1} (Fig. 2h).

The comparison in Fig. 2 between radar reflectivities and the objective precipitation partition algorithm demonstrates that even with hurricane force tangential flow, the objectively classified precipitation modes look reasonable compared to subjectively analyzing the data. Additionally, the precipitation partition is reasonably related to vertical velocity distributions (discussed further in section 3). Along with the algorithm's use for a satellite-based composite study by Tao and Jiang (2015) as well as for case studies of tropical cyclone Hermine (tropical storm strength) in Rogers et al. (2020) and for Hurricane Katrina in Didlake and Houze (2009), this analysis warrants the algorithm's further use in evaluating precipitation distributions.

3. Results

a. General characteristics of precipitation mode in tropical cyclones

Each grid point of the partitioned precipitation data were put into polar coordinates by assigning a radius and azimuth.

The radial coordinate was then normalized relative to the RMW which is deemed best because it accounts for differences in storm size and has been routinely used in composite airborne radar studies (e.g., Rogers et al. 2013b), but can lead to some uncertainty with respect to where a given precipitation mode is relative to the RMW with height because of differences in eyewall slope (e.g., Hazelton and Hart 2013) as well as uncertainty in estimating the RMW using the radar data. The partitioned reflectivities (from the radar swaths) were grouped into radial bands (radial grid spacing is $r^* = 0.25$ where $r^* = $ radius/RMW) regardless of azimuthal location. Throughout this manuscript, we define the eyewall region as the radial bands between $r^* = 0.75$ and $r^* = 1.25$. To examine the radial structure and frequency of each precipitation mode[3] in hurricanes, the data distribution is normalized by the total number of data points in the database (Fig. 3a), which shows the occurrence of each precipitation type relative to all precipitation modes (such that the sum of all bars in the plot is 1).

It is worth noting that comparison between inner and outer radii needs to be interpreted with caution since, due to the nature of polar coordinates, radial bands encompass a greater area at larger radii. Normalizing by the total number of data points within $r^* = 5$ shows that the most frequent precipitation mode is stratiform precipitation, comprising 82.6% of all precipitation within hurricanes (Fig. 3a). Stratiform precipitation's occurrence is most frequent in the radial band centered on $r^* = 1.25$ (all radial bands are centered on $0.25r^*$ increments such that this radial band is between $r^* = 1.125$ and $r^* = 1.375$) with 6.9% of all observed precipitation within the hurricane occurring here. The occurrence of stratiform precipitation steadily decreases with increasing radius away from the eyewall. In the radial band centered on $r^* = 1$, moderate convection is the most frequent mode of convection (~1.6% of all observed precipitation), followed by shallow convection (~0.7% of all observed precipitation). Deep convection, which is the least prevalent type of convection in the eyewall region (0.35% of all observed precipitation), becomes a negligible precipitation mode (<0.01% of all observed precipitation occurs in a single radial band) radially outward of $r^* = 2$.

The data distribution is also normalized by the number of data points of each precipitation mode (Fig. 3b; such that the sum of all bars in each mode is 1), which shows the radial distribution of each precipitation mode, regardless of their absolute frequency. Deep convection peaks in the radial bands centered on $r^* = 1$ and $r^* = 1.25$ (47.1% of all deep convection is in this region) with a sharp decrease in occurrence with increasing radius. Moderate convection also peaks in the radial band centered on $r^* = 1$ (16.4% of moderate convection is in this radial band), while shallow convection peaks radially inward in the radial band centered on $r^* = 0.75$ (13.9% of

---

[2] Of note, we considered building upon the existing algorithm to include a kinematic metric (vertical velocity or divergence) to the classify the precipitation structures, but did not include it in the analysis since it would make the comparison between airborne and satellite-base studies less direct and would significantly reduce our database size since it would only allow cases from 2010 and later due to an issue with the processing [discussed further later and in Fischer et al. (2022)].

[3] Note that Fig. 3 and the rest of the figures in the manuscript only include grid points with precipitation. Grid points characterized as "weak echo" were not included in this analysis because of potential biases of some P-3 missions happening to sample more dry regions in a TC. Therefore, weak echo classifications are treated the same as no observed precipitation (or no scatterers) and are not used for precipitation distributions.
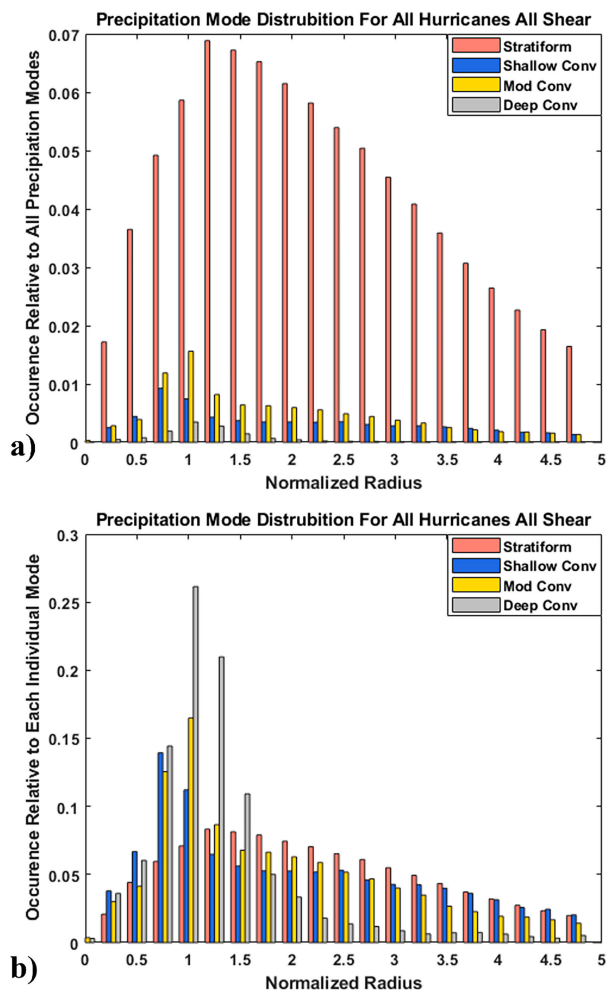
FIG. 3. Radial distributions (normalized radius = radius/RMW$_{2KM}$) of the four precipitation modes (stratiform precipitation, shallow convection, moderate convection, and deep convection), regardless of azimuthal storm-relative location. (a) The data are normalized by the total number of precipitation data points in the database. (b) The data for each precipitation mode are normalized by the total number of data points for that precipitation mode.

shallow convection is in this radial band). Of all the convective modes, shallow convection is spread most evenly throughout all radial bands, especially outside of $r^* = 2.5$. Stratiform precipitation peaks just outside the eyewall, in the radial band centered on $r^* = 1.25$, and, with no more than 10% of its occurrence in any radial band, is the most evenly distributed precipitation mode across radial bands. The radial distributions of convective and stratiform precipitations match well with an analysis of reflectivity distributions of Hurricane Alicia by Marks and Houze (1987; see their Fig. 9a), even though that study did not explicitly categorize precipitation modes. Note that since the amount of precipitation decreases substantially radially outwards of $r^* = 3$, and that there are no significant differences in the distribution of precipitation modes at those radii, the remaining analysis focuses on data radially inwards of $r^* = 3$.

b. Precipitation properties in intensifying, weakening, and steady-state hurricanes

1) RADIAL DISTRIBUTIONS

With the generalized precipitation distributions shown in the previous section, we now examine how those distribution change when considering a storm's subsequent intensification rate. Swaths from hurricanes in the TDR database are parsed into storms that underwent 12-h subsequent WE, INT, and those that maintained SS intensity. There are 128, 190, and 253 swaths from WE, INT, and SS hurricanes, respectively. To ensure equal comparison of the groups, for the summary statistics of each intensity change category, we only count each mission once. The WE and SS hurricanes have a mean initial intensity of 107 and 98.9 kt, respectively, while the INT hurricanes have an initially lower intensity at 92.7 kt (Fig. 4a). Unsurprisingly, INT hurricanes experience the most favorable mean environmental conditions of the intensity change groups including a lower shear magnitude (Fig. 4b) than the WE and SS hurricanes. The mean deep-layer wind shear for INT, SS, and WE hurricanes are 12.7, 15.3, and 16.0 kt, respectively. Using the Student's t test, the shear magnitude differences between INT and both WE and SS hurricanes are statistically significant for at least the 90% confidence interval. The mean SST for INT, SS, and WE hurricanes (Fig. 4c) are 29.2°, 29.0°, and 28.9°C, respectively. The mean low-level RH values are 67.5%, 67.4%, and 66.6% for INT, SS, and WE hurricanes, respectively (Fig. 4d). None of the SST and RH differences are statistically significant. Note that similar statistical differences are observed between the intensity change groups in the midlevels (700–500 mb; not shown). While there are some differences in environmental conditions between INT, SS, and WE cases, these are not large, and likely do not fully explain the differences in the TCs' varying intensity changes.[4]

As was done in Fig. 3, the precipitation partitions are put into radial bands ($r^* = 0.25$ grid spacing) regardless of azimuthal location, but now the data are also separated by a storm's intensity change category. Here, and throughout the rest of the manuscript, the data are normalized relative to the total number of grid points in a radial band to describe the relative contribution of each precipitation mode at each radius (such that the sum of all the bars in each radial band is 1; Fig. 5). The normalization allows us to focus on the radial structure of the relative importance of different precipitation modes across different storm groups. For all intensity change categories the radial bands centered on $r^* = 0.75$ and $r^* = 1.0$ are most convective (Fig. 5a) with less than 75% of the precipitation identified as

---

[4] Since the Student's t test implicitly assumes the samples are normally distributed, which is not necessarily the case for our samples, we also compared each distribution using a Wilcoxon rank sum test (equivalent to a Mann–Whitney U test), which is a nonparametric test on independent samples that does not depend on a normal distribution. All of the conclusions from that test are the same except for Fig. 4b where under the Wilcoxon test, the comparison between INT vs WE storms would be statistically significant at the 90% confidence interval (in the t test there is no statistical significance).
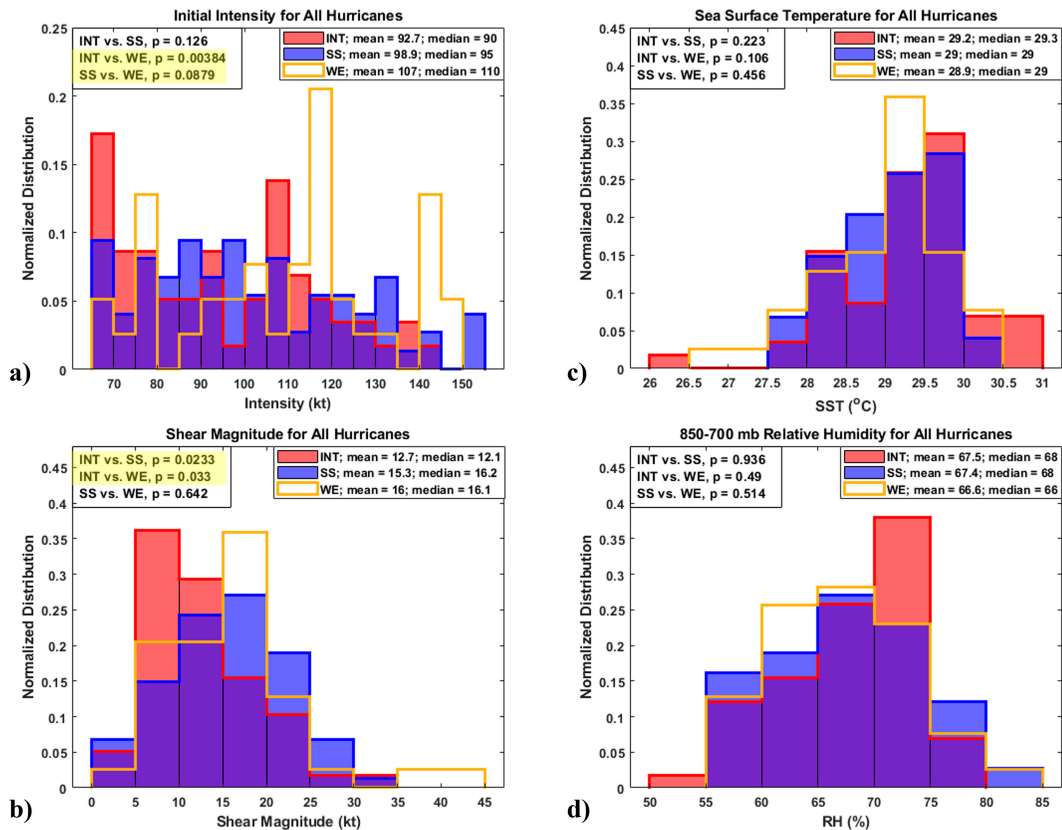
FIG. 4. Normalized distributions of (a) initial hurricane intensity, (b) 850–200-mb environmental wind shear magnitude, (c) sea surface temperature, and (d) 200–800-km area averaged relative humidity between 850 and 700 mb for hurricanes that underwent subsequent weakening (WE), maintained steady-state intensity (SS), and underwent subsequent intensification (INT). All panels are based on data obtained from the SHIPS database from the closest in time 6-hourly analysis. In each panel, mean and median quantities are noted for the three intensity change categories. Additionally, the p values from a Student's t test from comparing all the intensity change categories are noted in each panel with statistical significance at greater than the 90% confidence interval highlighted in yellow.

stratiform. In the radial band centered on $r^* = 1.0$, SS hurricanes are the least convective with 71.8% of observed precipitation in each radial band being stratiform rain. In contrast, only 64.6% of observed precipitation in this radial band is stratiform in INT hurricanes, potentially signifying stronger updrafts and a higher amount of mid and upper-level latent heating in the eyewall (discussed further below).

Out of all the convective modes, the greatest differences in the distributions near the eyewall are for shallow convection and deep convection (Figs. 5b,d). Shallow convection is most prevalent in INT hurricanes in radial bands centered between $r^* = 0.25$ and $r^* = 1.5$, and is maximized in the radial band centered on $r^* = 0.75$ (the radial band with its highest concentration regardless of intensity change; Fig. 3b). In that radial band shallow convection accounts for 14.7% of the observed precipitation in that band of INT hurricanes and only 12.0% of the observed precipitation in that band of SS and WE hurricanes.

In the radial bands between $r^* = 0.75$ and $r^* = 1.0$ of INT hurricanes, deep convection accounts for 3.6% and 5.5% of the observed precipitation in those radial bands, respectively

(Fig. 5d). In both those bins, deep convection in INT hurricanes is at least 50% more frequent than in SS and WE hurricanes. The difference in deep convection between the intensity change categories decreases with increasing radius. The higher concentration of convection (deep convection in particular) radially inwards of the RMW for INT hurricanes, is a signature hypothesized to be favorable for intensification since diabatic heating throughout the column is larger inside the region of highest vorticity (e.g., Vigh and Schubert 2009; Pendergrass and Willoughby 2009). These differences are consistent with the composite results of extreme updrafts (i.e., convective bursts) using the TDR database in Rogers et al. (2013b) and expand those results to show that deep convection in the eyewall is the predominant separator between intensity change categories, even when other precipitation modes are included (albeit there is some signal for shallow convection). Since Rogers et al. (2013b) did not explicitly analyze other precipitation modes, the particularly high significance of deep convection over other precipitation modes shown in this study demonstrates the importance of heating and humidification throughout the entire column of the

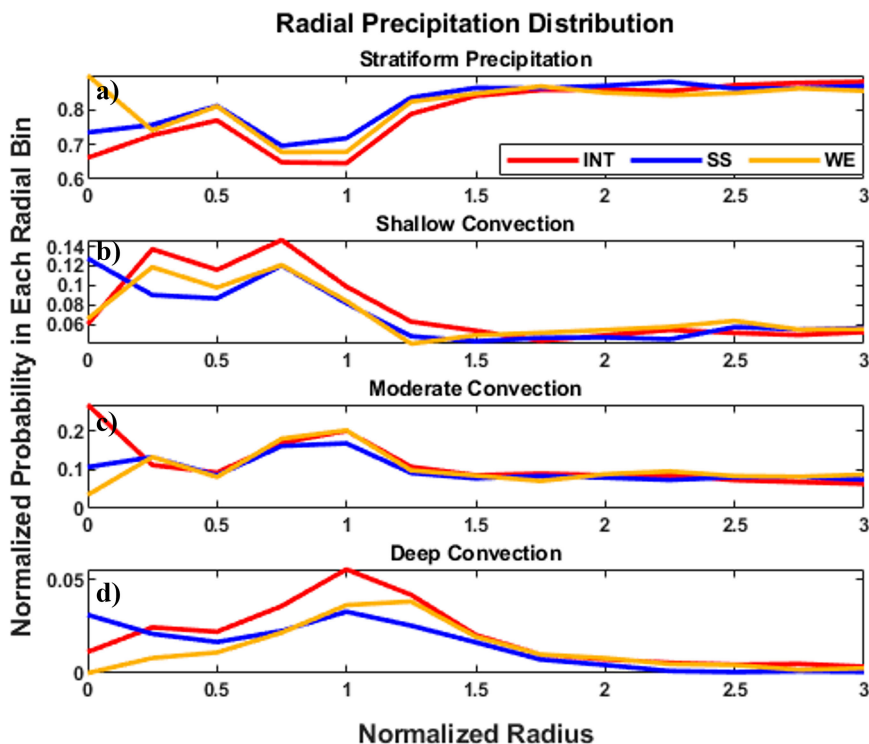## Radial Precipitation Distribution

FIG. 5. Radial distributions (regardless of azimuthal storm-relative location) of the four precipitation modes: (a) stratiform precipitation, (b) shallow convection, (c) moderate convection, and (d) deep convection for INT, SS, and WE hurricanes. Each radial band is normalized by the total number of grid points in that bin. To highlight differences, note that the ordinate axis is different in each panel and that the abscissa is zoomed in to be outward bounded by $r^* = 3$.

eyewall region, particularly radially inwards of the RMW. The enhanced heating associated with the deep convection can lead to the formation of a stronger TC warm core aloft and associated pressure falls compared to if the heating was radially outwards of the RMW (e.g., Nolan et al. 2007).

2) SHEAR-RELATIVE AZIMUTHAL DISTRIBUTIONS IN THE EYEWALL REGION

To explore whether differences in the radial distributions of each precipitation mode are related to systematic differences in the azimuthal precipitation structure, the data are further divided into both radial bands and shear-relative quadrants. The greatest azimuthal differences in the precipitation modes between the intensity change categories occur in the eyewall region. Therefore, the precipitation mode data were grouped into azimuthal bins of 30° for grid points between those radial bounds (Fig. 6). In INT hurricanes, deep convection (Fig. 6a) in the eyewall is most frequent left-of-shear with 44.3% of all deep convection in INT hurricanes occurring between 60° and 180° to the left of the shear vector. There is a fairly uniform distribution of deep convection at other azimuths in INT hurricanes. In contrast to INT hurricanes, deep convection in WE hurricanes occurs primarily in the DSL quadrant. This quadrant of WE hurricanes contains the highest concentration of deep convection of any intensity change category with

43.8% of all deep convection for those storms. While not as concentrated as in WE hurricanes, deep convection also peaks in the DSL quadrant in SS storms with 39.2% of eyewall deep convection in these storms. Because of the high concentration in the DSL quadrant, both WE and SS hurricanes have about half the relative frequency of eyewall deep convection in the upshear and right-of-shear quadrants as the INT storms. To test whether the differences in the distributions of Fig. 6a are statistically significant, we use a two-sample Kolmogorov–Smirnov (KS; Massey 1951) test which determines whether two samples come from the same distribution. Based on the KS test, each of the distributions are statistically significantly different at greater than the 99% confidence ($p < 0.01$), meaning that there is statistical confidence that the distributions of deep convection are different between intensity change categories.

The previous results suggest greater rates of TC intensification are associated with more symmetric distributions of deep convection, which is now quantitatively examined using a symmetry index. In a storm with perfectly symmetrically distributed precipitation mode, there would be an 8.3% occurrence in each 30° azimuthal bin (12 total bins). Therefore, to objectively determine how asymmetric precipitation distributions are, we will use the mean absolute difference from 8.3% occurrence (i.e., take the mean of all absolute value differences between the actual occurrence and 8.3%). For deep convection in the eyewall
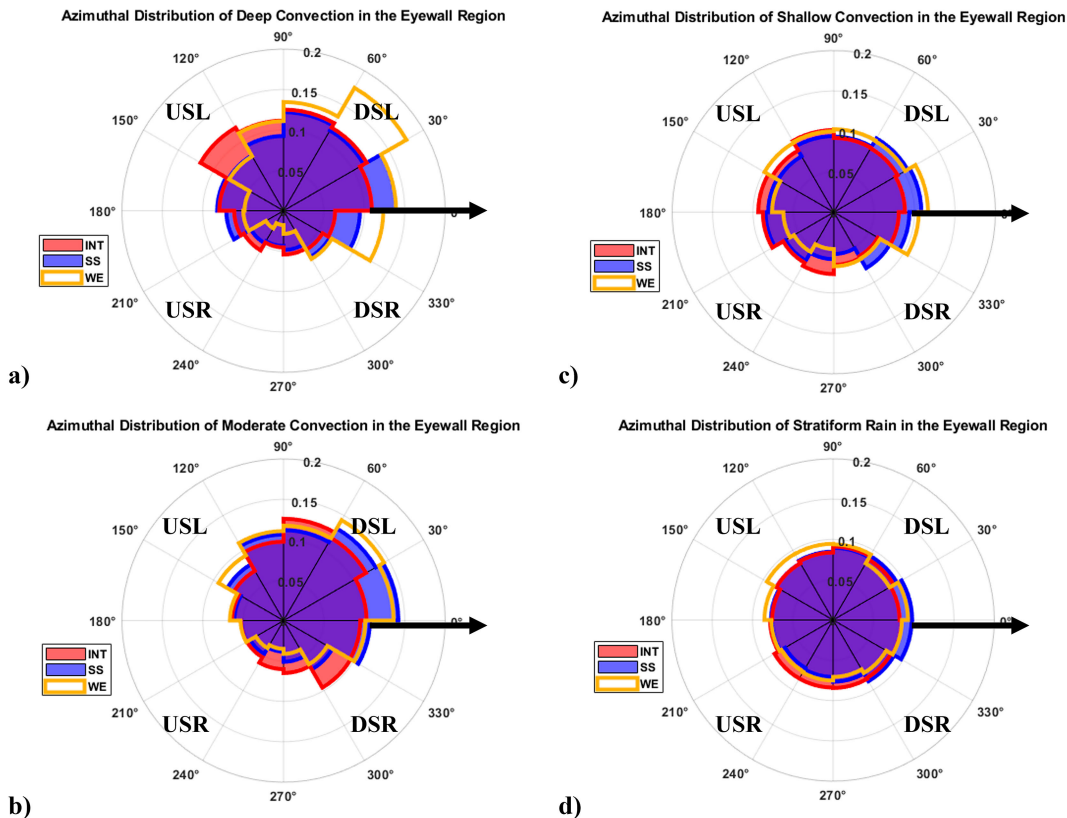
FIG. 6. Polar histograms showing the azimuthal distributions of (a) deep convection, (b) moderate convection, (c) shallow convection, and (d) stratiform precipitation relative to the environmental wind shear for data points in the eyewall region (between $R/\mathrm{RMW}_{2KM} = 0.75$ and $R/\mathrm{RMW}_{2KM} = 1.25$). In polar histograms, a larger radial component indicates a greater frequency. With 30° bins, an 8.3% occurrence in each bin represents a fully symmetrically distributed field. The data are normalized such that the sum of all the 30° bins for each intensity change category is 1.

region, the mean absolute difference from a symmetric distribution is 2.6%, 2.7%, and 4.2% for INT, SS, and WE hurricanes, respectively. This indicates that deep convection near the eyewall is more symmetrically distributed in INT and SS storms than WE storms, a pattern noticed to be favorable in many observational (e.g., Stevenson et al. 2014, 2018; Zagrodnik and Jiang 2014; Alvey et al. 2015; Rogers et al. 2013b, 2015, 2016; Rios-Berrios and Torn 2017; Wadler et al. 2018b, 2021b; Fischer et al. 2018) and modeling studies (e.g., Chen and Gopalakrishnan 2015; Onderlinde and Nolan 2014, 2016; Rios-Berrios et al. 2016a,b; Leighton et al. 2018; Zhang and Rogers 2019; Hazelton et al. 2021). This builds upon the results from the previous section which suggest that the distributions of latent heating and humidification throughout the column associated with deep convection favors intensification, particularly when it is symmetrically distributed inside of the RMW and occurs particularly in the upshear quadrants.

The cause for the greater frequency of deep convection in the USL quadrant of INT cases is unclear. We speculate that the upper-level thermodynamic conditions in the upshear quadrants (which could be modulated by ventilation) are more favorable for convection to persist in INT storms than in WE and SS storms which allows for more vigorous upper-level updrafts in

that region (e.g., Zawislak et al. 2016; Rogers et al. 2016), but that would need to be evaluated using numerical simulations or via case studies with adequate thermodynamic observations. It is also possible that the differences in the convective structure between the intensity change groups are influenced by different vortex tilt structures (e.g., Reasor and Eastin 2012; Reasor et al. 2013; Tao and Jiang 2015; Rios-Berrios et al. 2018; Alvey et al. 2020; Boehm and Bell 2021; Ryglicki et al. 2021; Schecter 2022; Yu et al. 2023). However, an initial search of the hurricanes examined here found no significant relationship between the rate of TC intensity change and vortex tilt magnitude (not shown), consistent with the findings of Rogers et al. (2013b).

The second most asymmetrically distributed precipitation mode is moderate convection (Fig. 6b). All intensity change categories have a higher percentage of moderate convection in the left of shear semicircle than in the right of shear semicircle. The mean absolute difference from symmetrically distributed moderate convection is 1.8%, 2.9%, and 3.2% for INT, SS, and WE hurricanes, respectively. However, the differences in the distribution of moderate convection between the intensity change groups are not as systematic as for deep convection. This suggests that the latent heating and humidification associated with the strongest updrafts at high altitudes

are more important for intensification than weaker updrafts at low altitudes. Alternatively, this can suggest that that ventilation and/or forcing for ascent in the lower troposphere is what independently governs how deep and vigorous convection becomes.

Shallow convection (Fig. 6c) and stratiform precipitation (Fig. 6d) contain comparatively small, but consistent differences between the azimuthal distributions in the eyewall region. There is consistently more shallow convection in the upshear and right of shear region (between 150° and 270° to the left of the shear vector) of INT hurricanes than SS and WE hurricanes. Interestingly, stratiform precipitation has the most symmetric distribution of all the precipitation modes. The mean absolute difference from symmetrically distributed stratiform precipitation is 0.34%, 0.52%, and 0.85% for INT, SS, and WE hurricanes, respectively.

Overall, Fig. 6 indicates that convection (particularly deep convection) is more symmetrically distributed around the eyewall in INT hurricanes than SS and WE hurricanes. Interestingly, the differences in the azimuthal distribution of stratiform precipitation are less significant than what was found in the satellite-based studies such as Tao et al. (2017), which found that intensification was associated with an increase in stratiform precipitation in all azimuths, but especially the USL quadrant. However, Tao et al. focused primarily on the innermost 100-km and not the eyewall region since satellite-based fields do not have kinematic information about a TC such as the RMW. Tao et al. also considered weaker TCs which are usually more asymmetric and compared the distributions relative to the time of RI onset which is beyond the scope of this manuscript due to the limited size of the TC-RADAR database. Additionally, there may be discrepancies due to differences in swath coverages as Tao et al. only required that TRMM precipitation radar passes cover at least 50% of the storm while TDR measurements on P-3 missions typically capture all azimuths around the eyewall region.

The differences in the azimuthal distribution of precipitation modes (particularly deep convection) near the eyewall in Fig. 6 imply that there are fundamental differences in the distribution of strong vertical velocities near the eyewall between intensity change groups. Contoured frequency by altitude diagrams (CFADs; Yuter and Houze 1995; Hence and Houze 2008) are created for the eyewall region (same radial criteria as Fig. 6) of each shear-relative quadrant with the differences between INT and WE hurricanes shown in Fig. 7.[5] Note that Fig. 7 only contains data after 2010 due to an issue with the vertical velocity retrieval prior to that year [which did not influence the reflectivity and precipitation mode analysis; see Fischer et al. (2022) for discussion about the vertical velocity retrieval in the TC-RADAR database].

In the DSR quadrant (Fig. 7d), WE hurricanes have a greater occurrence of positive vertical velocities greater than

---

[5] Note that since Fig. 7 shows differences, the positive (red) colors represent a higher frequency in INT hurricanes while cooler (blue) colors represent a higher frequency in WE hurricanes. For all the quadrants, similar, though not as extreme, differences are noticed between INT and SS hurricanes (not shown).
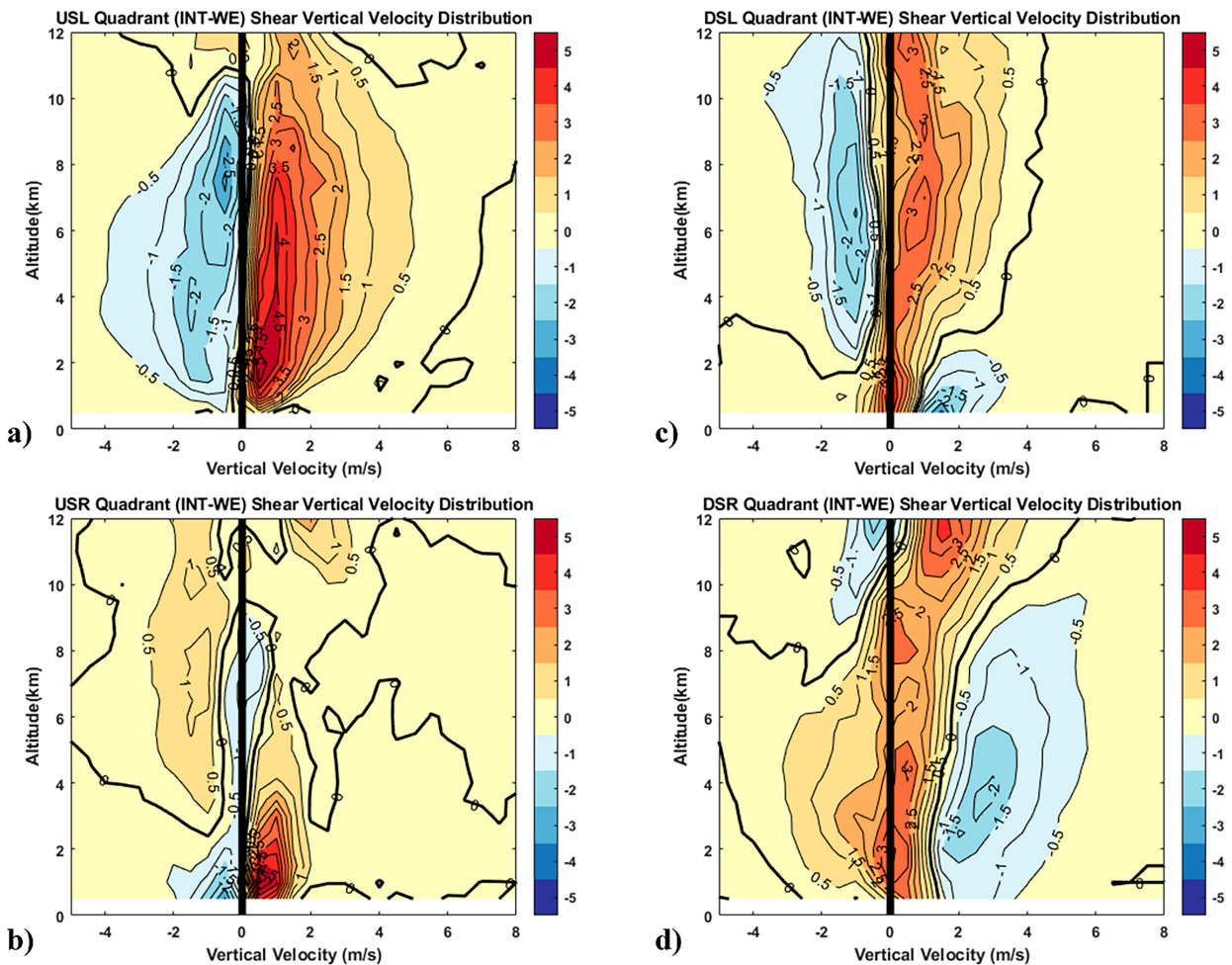
1.5 m s^{-1} between 0.5- and ~10-km altitude. In this quadrant, the greatest difference in vertical velocity frequency between the INT and WE hurricanes is between 2 and 4 m s^{-1} and at altitudes between 4 and 5 km. The stronger updrafts in the DSR quadrant are likely associated with the higher concentration of deep convection in the downwind DSL quadrant of WE hurricanes (i.e., Fig. 6a). The differences between INT and WE hurricanes reverse in the DSL quadrant (Fig. 7c), where WE hurricanes favor midlevel downdrafts, mainly between 3- and 9-km altitude, and between −2 and 0 m s^{-1}. INT hurricanes favor updrafts greater than 1 m s^{-1} above 2.5-km altitude in the DSL quadrant, signaling the favorability for deep convection downwind in the USL quadrant. The downwind shift in deep convection is likely because many hydrometeors above the freezing levels are low-density (Houze et al. 1992; Black et al. 1996) which means they have a longer residence time and can be advected farther around the storm by the tangential winds (called the "mixmaster" effect; Marks and Houze 1987; Rogers et al. 2009).

The greatest differences in updraft distributions between INT and WE hurricanes are in the USL quadrant (Fig. 7a). At nearly all altitudes of this quadrant, there is a stronger preference for updrafts in INT than WE hurricanes. The differences in positive vertical velocities are maximized between 2- and 6-km altitude and vertical wind speeds between 1 and 2 m s^{-1}. In contrast, WE hurricanes have a strong preference for downdrafts above 2-km altitude in this quadrant, a signature that could represent a greater transport of low entropy air toward the boundary layer (e.g., Riemer et al. 2010) which is generally assumed to occur in the primary rainband but has been also observed in the eyewall region (Wadler et al. 2018a). Less significant differences are present in the USR quadrant (Fig. 7b), though INT hurricanes favor positive vertical velocities below 2-km altitude and between 0 and 2 m s^{-1}, which is a potential indicator that convective initiation can occur in this quadrant. CFADs of divergence in this quadrant confirm that INT hurricanes favor more convergence between 1- and 5-km altitude in the USR quadrant than WE hurricanes (not shown).

c. Precipitation properties in TCs experiencing shear with northerly and southerly components

As described earlier, a recent study by Wadler et al. (2022) showed, using two independent observational databases, that when TCs experience southerly component shear, a 4–6-K wavenumber-1 asymmetry in boundary layer θ_e (through atmospheric moisture) exists between the left-of-shear and right-of-shear quadrants (higher values right-of shear). This thermodynamic asymmetry was less pronounced for TCs experiencing shear with a northerly component. To determine whether those differing thermodynamic distributions affect precipitation structures, the partitioned precipitation data are recategorized for hurricanes experiencing deep-layer environmental wind shear with a northerly component (heading greater than 90° and less than 270°) and a southerly component (heading greater than 270° and less than 360°; also greater than 0° and less than 90°), regardless of intensity

FIG. 7. The difference in contoured frequency by altitude diagrams (CFADs; Yuter and Houze 1995; Hence and Houze 2008) of vertical velocity (bin size is 0.5 m s^{-1}) between INT and WE hurricanes in the (a) upshear-left, (b) upshear-right, (c) downshear-left and, (d) downshear-right quadrant for all data points in the eyewall region (between R/RMW$_{2KM}$ = 0.75 and R/RMW$_{2KM}$ = 1.25). In each panel, zero vertical velocity is outlined in a thick vertical line while the zero difference contour is in bold.

change. There is a fairly equal distribution of shear headings of hurricanes sampled in the TC-RADAR database with a northerly and southerly component (Fig. 8), with over 75% of shear headings toward the east.

The favorably symmetric (northerly component shear) and unfavorably asymmetric (southerly component shear) thermodynamic distributions are echoed in the precipitation distributions in Fig. 9 which divides the precipitation data within the eyewall region data into the same 30° azimuthal bins as in Fig. 6. Hurricanes experiencing northerly component shear have a higher amount of deep convection in every quadrant except the DSR quadrant (22.8% of all deep convection is in the DSR quadrant of southerly component shear as opposed to 15.9% in northerly component shear cases) (Fig. 9a). Besides the DSR quadrant, the greatest difference in deep convection between northerly component and southerly component shear cases is in deep convection in the USL quadrant. The lower amount of deep convection in this region for southerly component shear

cases is potentially a downwind effect resulting from the lower boundary layer θ_e values in the left-of-shear quadrants shown in Wadler et al. (2022) for these cases [a process discussed in Rogers et al. (2016) for Hurricane Edouard of 2014]. However, a numerical modeling study is needed to evaluate processes leading to the different deep convective distributions.

While moderate convection (Fig. 9b) and stratiform precipitation (Fig. 9d) do not have systematic differences between the shear direction groups, there are noticeable differences in shallow convection (Fig. 9c), with a slight, but consistently higher concentration of shallow convection upshear (between 150° and 210° to the left of the shear vector) in the southerly component shear cases. Using a KS test, both distributions in Figs. 9a and 9c are statistically significant different between northerly component and southerly component shear at greater than 99% confidence. We speculate that the lower boundary layer θ_e values in the left-of-shear quadrants of southerly component shear cases lead to less instability in convective cores such that they
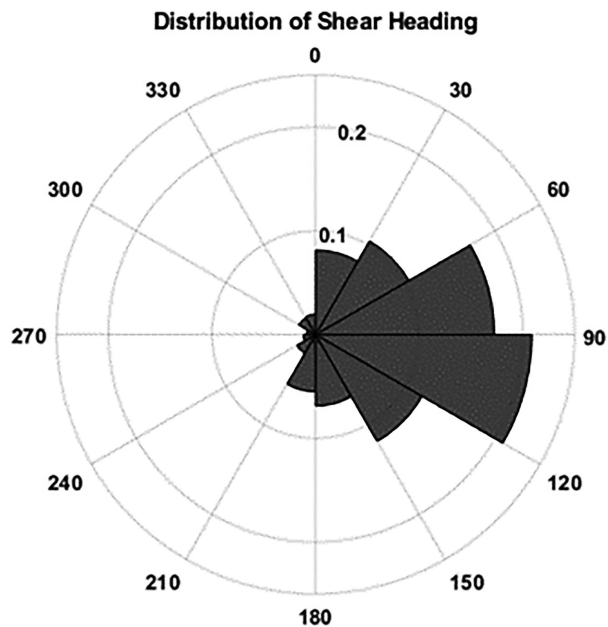
FIG. 8. Polar histograms showing the azimuthal frequency of deep-layer wind shear headings for all TC cases examined in this study. The data are normalized such that the sum of all the 30° bins is 1.

peak at a lower altitude in the upshear region of the eyewall. Note that the results shown in Fig. 9 are not sensitive to the definition of northerly component and southerly component shear, as a 20° buffer room between them such that if the northerly component headings are between 110° and 260° and southerly component headings are between 280° and 360° and between 0° and 80°, the results are similar (not shown).

Interestingly, the differences in the azimuthal distribution of the precipitation modes in the eyewall region between hurricanes experiencing northerly component and southerly component shear (Fig. 9) largely reflect the differences between INT and WE hurricanes (Fig. 6). Given that the distributions are derived from the same precipitation database, the more favorable precipitation distributions for hurricanes in the TDR database that experience northerly component shear are associated with preferential subsequent 12-h intensification (Fig. 10a). Subsequent 12-h intensity increases changes between 5 and 20 kt favor hurricanes experiencing northerly component shear, while subsequent intensity changes between −20 and −5 kt favor southerly component shear, even though the mean initial intensities are similarly near 95–100 kt between the two groups (Fig. 10b). Using the Student's t test, the differences in the intensification rate are statistically significant at greater than the 99% confidence interval, consistent with the TC climatology distributions derived from the SHIPS database in Wadler et al. (2022). Of note, as with Fig. 4, all statistical comparisons in Figs. 10 and 11 are with one swath per storm to ensure all storms are weighted equally. While the differences in intensification rate between the two shear direction groups are likely associated with the differences in precipitation and their respective projections of latent heating on the

wavenumber-0 structure (Nolan et al. 2007), the greater amount of deep convection in the left-of-shear quadrants and greater TC intensification rates observed in northerly component shear cases seems to be due to the boundary layer thermodynamic distributions shown in Wadler et al. (2022). The mean wind shear magnitude in the northerly component cases (14 kt) is relatively similar (and not statistically significantly different) to that in the southerly component flow sample (15 kt; Fig. 10c).

Results derived from the SHIPS developmental database in Wadler et al. (2022) also showed that the greatest difference in intensification rates between northerly component and southerly component wind shear are when hurricanes experience moderate magnitudes of vertical wind shear, defined as a shear magnitude between 4.5 and 11 m s^{-1} (Rios-Berrios and Torn 2017), an environmental regime that is difficult to accurately forecast in (Molinari et al. 2004, 2006; Molinari and Vollaro 2010; Montgomery et al. 2010; Bhatia and Nolan 2013; Foerster et al. 2014; Stevenson et al. 2014; Rios-Berrios et al. 2016b,a; Zawislak et al. 2016; Rios-Berrios and Torn 2017; Nguyen et al. 2017; Finocchio and Majumdar 2017; Rios-Berrios et al. 2018; Rogers et al. 2020). To examine how these climatological relationships between shear magnitude and intensification rate are related to the precipitation mode distributions, in the current study we further stratify the precipitation data by both the environmental wind shear magnitude and a hurricane's initial intensity (i.e., all hurricanes, only minor hurricanes, and only major hurricanes). The greatest overall differences in the intensification rates and precipitation structure are for major hurricanes experiencing moderate wind shear values (Fig. 11). Here, northerly component shear cases ($N = 70$ swaths) have a mean intensity change of 3.7 kt over the subsequent 12 h while southerly component shear cases ($N = 88$ swaths) have a mean intensity change of −5.9 kt over the subsequent 12 h (Fig. 11a). The differences in intensification rate are statistically significant at greater than 99% confidence interval. Interestingly, even though the mean initial intensity of major hurricanes cases in northerly component shear is 121 kt, 8 kt higher than the southerly component shear subsample (Fig. 11b), more than half of the northerly shear cases experience subsequent intensification. Of note, even though the shear magnitudes are limited to the moderate range, the mean is 14 kt (7.2 m s^{-1}) and 16 kt (8.2 m s^{-1}) for the northerly component and southerly component cases, respectively (not shown). We speculate that the difference in shear magnitude cannot be responsible for the different mean intensity changes and precipitation distributions between the shear direction groups. Note that similar results (though not as significant) are obtained for all hurricanes in moderate shear (not shown).

In terms of the precipitation distribution (Fig. 12a), the eyewall region of major hurricanes in moderate northerly component shear cases is significantly more convective (40.4% of grid points) than the major hurricanes in moderate southerly component shear cases (33.2% of grid points). The greater identification of convective points for northerly component shear cases spans all three convective modes signifying more heating and humidification at all levels in the eyewall region.
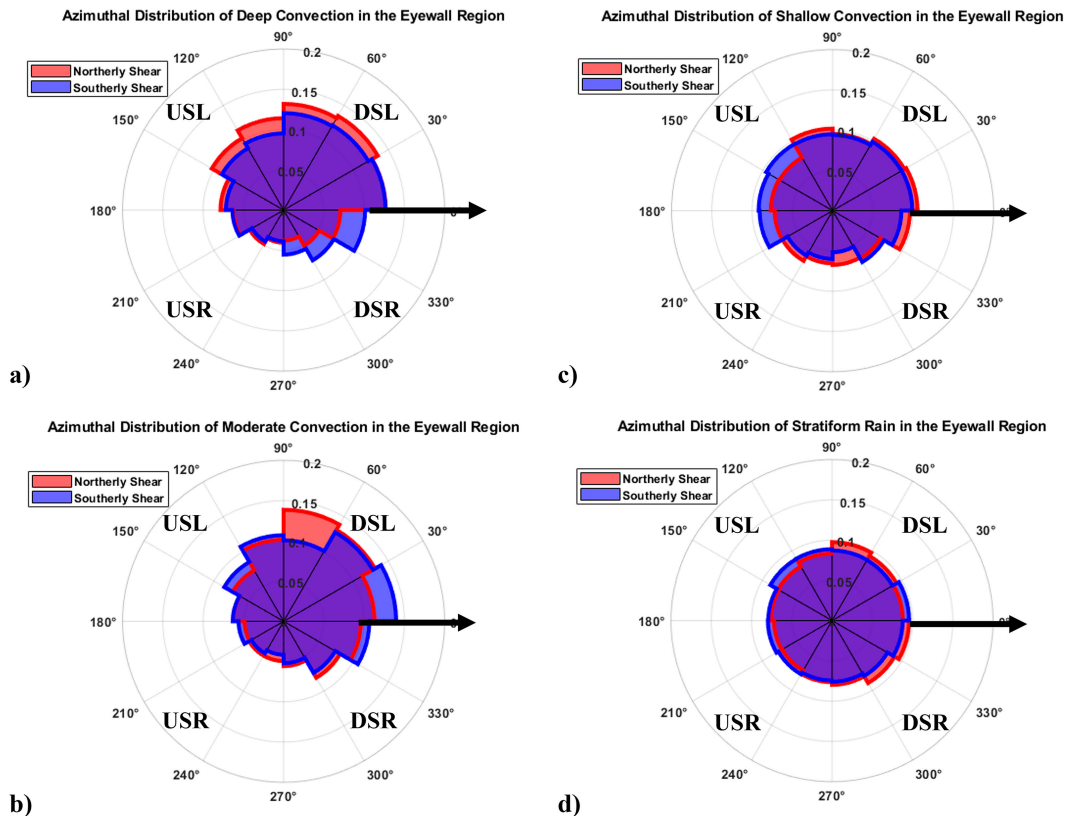
FIG. 9. Polar histograms showing the azimuthal distributions of (a) deep convection, (b) moderate convection, (c) shallow convection, and (d) stratiform precipitation for relative to the environmental wind shear for data points in the eyewall region (between $R/\text{RMW}_{2\text{KM}} = 0.75$ and $R/\text{RMW}_{2\text{KM}} = 1.25$) for hurricanes experiencing northerly component and southerly component deep-layer environmental wind shear. In polar histograms, a larger radial component indicates a greater frequency. With 30° bins, a 12% occurrence in each bin represents a fully symmetrically distributed field. The data are normalized such that the sum of all the 30° bins for each shear direction is 1.

The major hurricanes subsample experiencing a moderate amount of northerly component shear had a greater concentration of deep convection between 150° and 270° to the left of the shear vector, and a lower concentration of deep convection elsewhere (Fig. 12b). Deep convection is also more symmetrically distributed in the northerly component cases with a mean absolute deviation of 2.8% from a perfectly symmetric distribution average of 8.3% in each 30° azimuthal bin (mean deviation is 3.7% in southerly component shear cases). Significant differences between the groups also appear in the azimuthal distribution of moderate and shallow convection in the eyewall (Figs. 12c,d). Moderate convection is most prevalent in the downshear of southerly component shear cases. The largest concentration of shallow convection in northerly component shear cases also appears upshear.

As before, the differences in precipitation distributions reflect differences in the vertical velocity distributions. In the DSR quadrant, southerly component shear cases have a greater percentage of updrafts between 0.5- and 10-km altitude than the northerly component shear cases (Fig. 13d). The greatest differences in updraft distributions are between 0 and 4 m s^{-1}, likely highlighting the development of moderate

convection which peaks downwind in the DSL quadrant of the southerly component shear storms (Fig. 12c). The northerly component shear cases favor having stronger mid and upper-level updrafts in the left-of-shear quadrants (Figs. 13a,c) than the southerly component shear cases, with the differences maximized in the USL quadrant (Fig. 13a). As when comparing INT and WE hurricanes in Fig. 7a, northerly component shear cases have higher concentrations of positive vertical velocities between 2 and 8 km in the USL quadrant, while southerly shear cases have a significantly higher concentration of downdrafts at all altitudes. Additionally, as when comparing INT and WE hurricanes, northerly component shear cases have a higher amount of low-level (0.5–4 km) updrafts between 0.5 and 3 m s^{-1} (Fig. 13b), collocated with higher amounts of convergence (not shown), which signals a preferential region for convective initiation.

4. Discussion and summary

Airborne pseudo dual-Doppler radar data collected from hurricanes on the NOAA P-3 between 1997 and 2021 are partitioned into different precipitation modes (i.e., stratiform
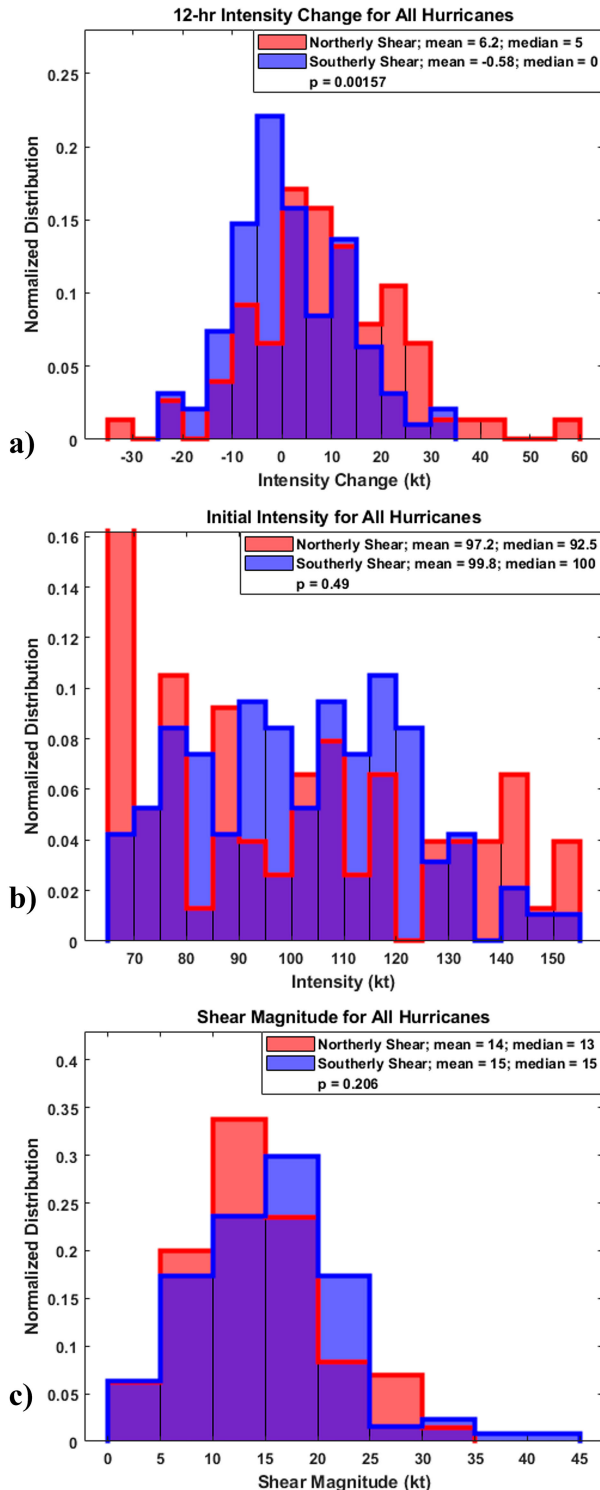
FIG. 10. Normalized distributions of (a) 12-h intensity change, (b) initial intensity, and (c) deep-layer wind shear magnitude for hurricanes experiencing northerly and southerly shear. The mean and median for each field is given in every plot.
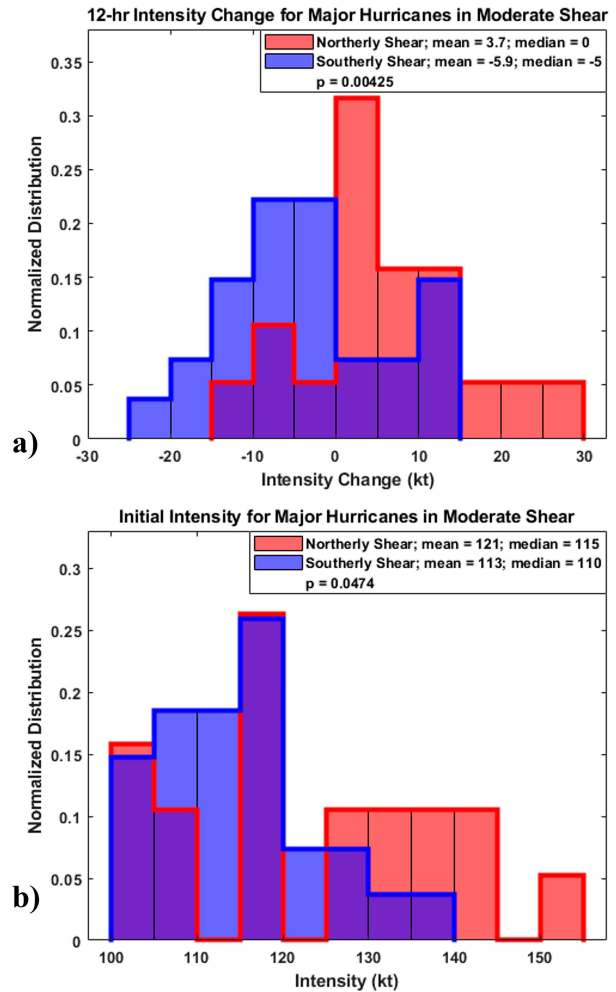

FIG. 11. (a),(b) As in Figs. 10a and 10b, but only for major hurricanes in moderate shear.

precipitation, shallow convection, moderate convection, and deep convection) to describe the relationship between precipitation distributions to hurricane intensity change and the horizontal direction of the 850–200-mb environmental wind shear vector. From all hurricanes, the most common precipitation mode within $r^* = 5$ is stratiform precipitation with 82.6% of all observed precipitation. Shallow, moderate, and deep convection constitute 6.6%, 9.5%, and 1.3% of all observed precipitation, respectively. Stratiform precipitation is the most uniformly distributed precipitation mode and peaks just radially outside the eyewall in the radial band centered on $r^* = 1.25$, while all the convective modes occur most frequently in the $r^* = 1$ radial band.

a. Precipitation distributions of intensifying, weakening and steady-state hurricanes

To elucidate how precipitation mode distributions are related to TC intensity change, the data were partitioned into INT, WE, and SS hurricanes. Among all the radial bands, the greatest differences in the areal coverage of the precipitation
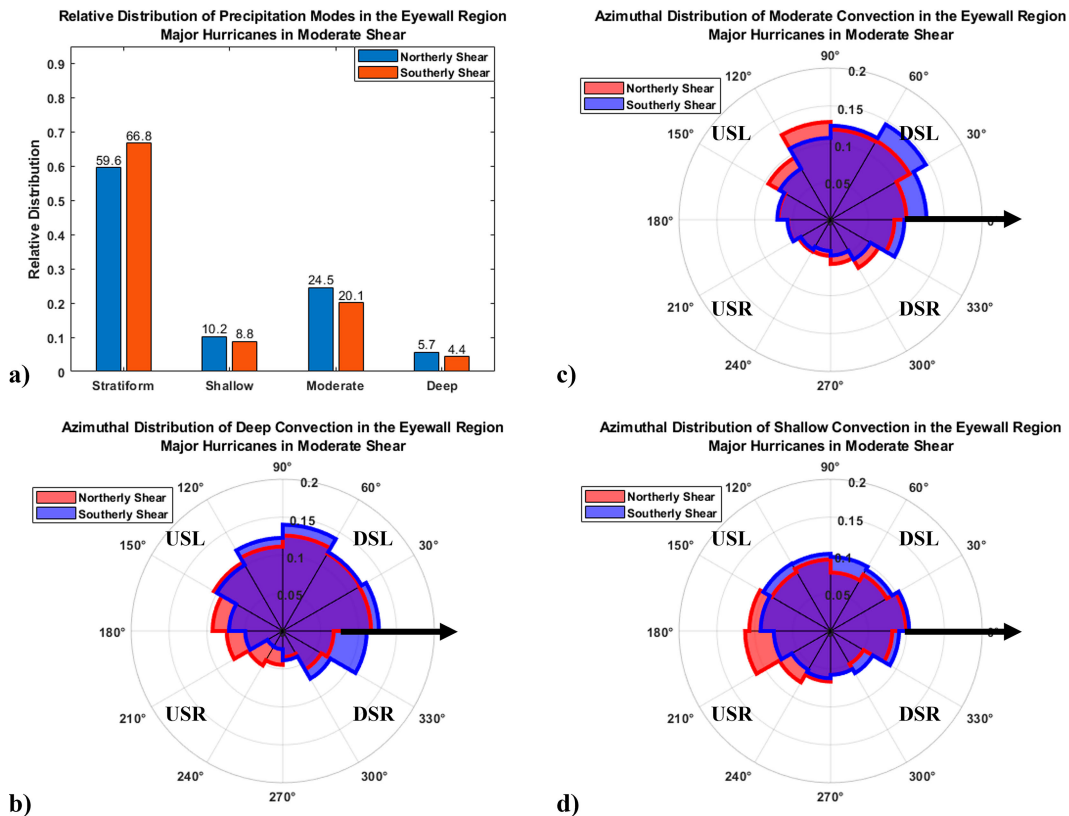
FIG. 12. (a) The percent of areal coverage of the four precipitation modes in the eyewall region. (b)–(d) As in Fig. 9, but for the comparison of (b) deep convection, (c) moderate convection, and (d) shallow convection between major hurricanes experiencing moderate amounts of northerly component and southerly component environmental wind shear.

modes are for deep convection between $r^* = 0.75$ and $r^* = 1.25$ (the eyewall region) where INT hurricanes have the greatest areal coverage of convection with 28.1% of grid points identified as convection. Overall, WE hurricanes have the least amount of deep convection for all radial bands inwards of $r^* = 1$, a signature noticed to be unfavorable for intensification since the diabatic heating is outside the region of highest vorticity (e.g., Vigh and Schubert 2009; Pendergrass and Willoughby 2009) which is an unfavorable configuration for the inward advection of absolute angular momentum (Smith and Montgomery 2016). This relationship between the radial distribution of deep convection and TC intensification has also been shown in modeling (Rogers 2010; Zhang and Chen 2012; Chen and Zhang 2013) and observational (Rogers et al. 2013b; Wadler et al. 2018b; Stevenson et al. 2018) studies.

With the greatest differences in the radial distribution of precipitation between the intensity change categories being in the eyewall region, the azimuthal precipitation structure in this region was explored. A summary schematic of the azimuthal differences is given in Fig. 14. INT hurricanes (Fig. 14a) have a more symmetric distribution of deep convection in the eyewall region than SS and WE hurricanes (Fig. 14b). In WE hurricanes, deep convection in the eyewall is mostly confined to the

DSL quadrant with 43.8% of all deep convection for those storms occurring in this quadrant. While not as extreme, 39.2% of all eyewall deep convection preferentially occurs in the DSL quadrant in SS hurricanes. In INT hurricanes, deep convection is most prevalent left-of-shear but is more symmetrically distributed than the other intensity change categories.

The distribution of deep convection has the most pronounced difference between the intensity change groups of any precipitation mode. This is an interesting result because while deep convection can be a significant source of vertical mass flux (Braun 2002), moderate and shallow convection have a greater areal coverage, which can lead to a greater aggregate contribution to latent heating and total volumetric rain rate (e.g., Tao and Jiang 2015). We speculate that the symmetric distribution of heating at all levels associated with deep convection in the eyewall is more important for intensification as compared to having heating limited to the low- and midlevels from weaker forms of convection and stratiform rain. The upper-level heating can lead to a stronger TC warm core aloft and associated pressure falls. Alternatively, the signals can suggest that that ventilation and/or forcing for ascent in the lower troposphere is what independently governs how deep and vigorous convection becomes [a similar conclusion to Rogers et al. (2016)]. A numerical modeling study specifically analyzing the effects of different
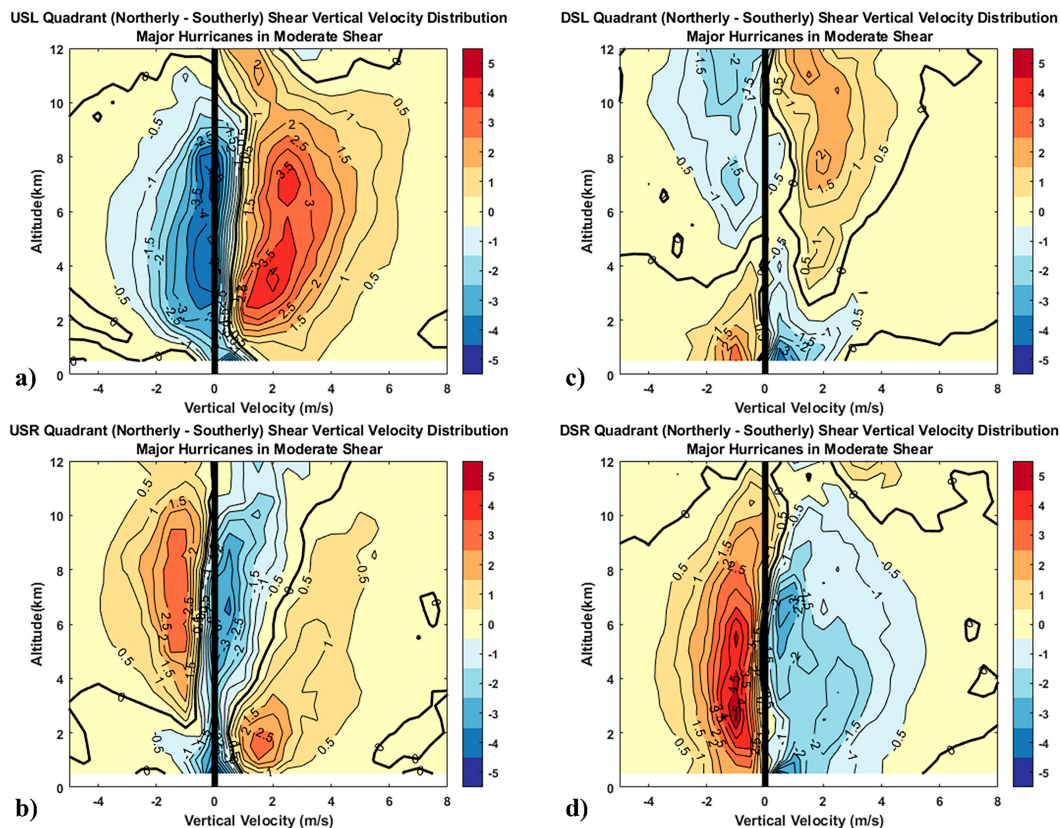
FIG. 13. As in Fig. 7, but for comparing major hurricanes (>50 m s^{-1} 1-min sustained winds at 10 m) experiencing moderate amounts (4.5–11 m s^{-1}) of vertical wind shear with a northerly and southerly component.

precipitation modes is needed to confirm this result. The more symmetric distribution of deep convection in INT hurricanes may also be an indicator of favorable tilt precession into the USL quadrant, which favors realignment (e.g., Stevenson et al. 2014; Munsell et al. 2017; Rios-Berrios et al. 2018; Alvey et al. 2020); however, such a shear-relative tilt configuration was rarely observed in the storms in the TC-RADAR database (Fischer et al. 2022). The relationship between vortex tilt and TC intensification using TC-RADAR is currently being explored in a separate study and the tilt direction in Fig. 14 should not be assumed constant.

The differences in the distribution of deep convection are generally downwind of differences in the vertical velocity distribution with WE hurricanes having a greater occurrence of positive vertical velocities greater than 2 m s^{-1} between the surface and 10-km altitude in the DSR quadrant. INT hurricanes have a greater prevalence of upper-level updrafts in all other quadrants. Thus, even though the majority of vertical velocities in the eyewall are composed of weak drafts (e.g., Jorgensen 1984; Jorgensen et al. 1985; Black et al. 1996; Rogers et al. 2006, 2012, 2013b; Fischer et al. 2022), differences in the stronger vertical motions have a more pronounced relationship to hurricane intensity change. We speculate that enhanced low-level buoyancy and convergence in the right-of-shear quadrants, as well as favorable upper-level thermodynamic conditions (such are more

humidity) in the upshear quadrants, allow for the vigorous updrafts and deep convection to persist into the upshear quadrants. The upper-level thermodynamic conditions in the upshear quadrants of WE and SS storms may limit the persistence of deep convection into the upshear semicircle (e.g., Chen and Gopalakrishnan 2015; Zawislak et al. 2016).

Interestingly, there are no significant differences in the distribution of stratiform precipitation between any of the intensity change categories, as opposed to what was shown for TCs undergoing RI in the satellite-based study by Tao et al. (2017). Previous studies of airborne Doppler radar analyses of intensifying TCs by Rogers et al. (2013b) and Wadler et al. (2018b) attributed differences between satellite-based and TDR-based distributions of deep convection to differences in the sample sizes of the datasets. Additionally, due to the size of the database, this study can only focus on the future change in TC intensity while Tao et al. (2017) was able to further stratify by TCs starting intensification and those continuing intensification. Since other potential causes for the differences are mean environmental differences between the studies based on the domains of sampled TCs (e.g., Harnos and Nesbitt 2016a,b; Fischer et al. 2018), different radar resolutions and calibrations, and our limiting this study to TCs with an initial intensity of hurricane strength or greater, case studies sampled by both platforms are needed to elucidate why there are discrepancies between the composite storm structures.

Intensifying Hurricanes

a)　　Overall: Greater overall presence of convection, especially in the upshear-left quadrant

Steady-State and Weakening Hurricanes

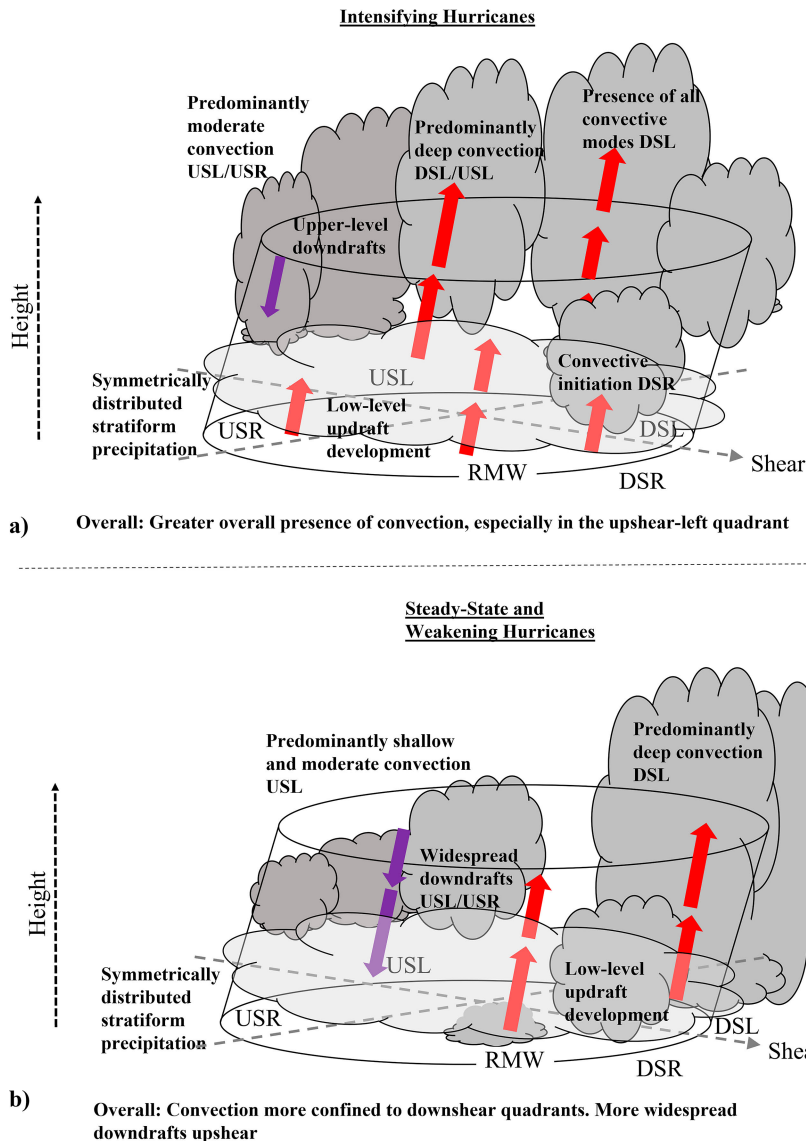b)　　Overall: Convection more confined to downshear quadrants. More widespread downdrafts upshear

FIG. 14. A schematic summary of the precipitation and vertical velocity distributions around the eyewall region of (a) intensifying hurricanes and (b) weakening and steady-state hurricanes. Red arrows indicate areas of predominantly rising motion while blue arrows indicate areas of predominantly sinking motion. The depth of the clouds is related to the type of precipitation, with the light flat cloud representing stratiform precipitation.

It is likely that INT hurricanes have vortex structures, such as the shape of the wind field (e.g., Zhang et al. 2023), that favor greater inflow and ascent. Additionally, INT hurricanes may be more convective near the eyewall because they have more favorable inner-core thermodynamic conditions and a tendency for more convergence at the base of the eyewall for both convection to form (for shallow convection) and for it to grow/propagate (for deep convection) than WE and SS hurricanes. Using a dropsonde database, Nguyen et al. (2019) found that for weak storms the difference in thermodynamic distributions is related to intensification rate, with more conditional instability downshear for intensifying storms. Nguyen

et al. linked the conditional instability to enhanced air–sea enthalpy fluxes upshear which is likely due to enhanced air–sea moisture disequilibrium in these storms (e.g., Cione et al. 2013; Jaimes de la Cruz et al. 2021).

b. Precipitation distributions of hurricanes experiencing northerly component and southerly component environmental wind shear

With the baseline precipitation distributions documented for INT, SS, and WE hurricanes, the precipitation database was also broken up into hurricanes that experience vertical wind shear with a northerly and southerly component. A

recent study by Wadler et al. (2022) showed that there is a 4–6-K wavenumber-1 asymmetry outside the inner-core in the boundary layer θ_e when TCs experience shear with a southerly component, while the boundary layer was more symmetric when TCs experience shear with a northerly component. How the boundary layer thermodynamic structures are related to precipitation distributions within the inner core remained an open topic that this study sought to address.

As with the comparison of the intensity change categories, the greatest differences in the precipitation distributions between the shear direction is for deep convection in the eyewall region. Hurricanes experiencing northerly component shear have more symmetric distributions of deep convection than hurricanes experiencing southerly component shear, which have deep convection preferentially confined to the DSR quadrant. The precipitation distribution in hurricanes experiencing northerly component shear generally resembles that for INT hurricanes in Fig. 14a while the precipitation distribution in hurricanes experiencing southerly component shear generally resembles that for WE/SS hurricanes in Fig. 14b. Likely because of these precipitation, and previously documented thermodynamic distributions that translate to the inner-core through the inflow layer [see Wadler et al. (2022) for the thermodynamic distributions], hurricanes experiencing northerly component shear tend to intensify (mean of 6.2 kt of intensity change in 12 h) while hurricanes experiencing southerly component shear tend to weaken (mean of −0.58-kt intensity change in 12 h). We hypothesize that the thermodynamically unfavorable air in the boundary layer right-of-shear in the southerly component shear cases is entraining into the eyewall and limiting the strength of the convection; however, numerical modeling and individual observational case studies are needed to diagnose the pathways air parcels travel as they spiral inward from outer radii. The greatest overall differences in the precipitation structures between the shear direction groups are for major hurricanes experiencing a moderate amount of vertical wind shear.

The results of this study emphasize that even though deep convection is the least frequent type of precipitation mode, at only 1.3% of all observed precipitation within $r^* = 5$, it is the differences in its distribution, especially azimuthally around the eyewall region, that is the greatest indicator of all precipitation modes for subsequent intensification. Thus, the distribution of deep convection could serve as information in a statistical predictive scheme such in SHIPS or a machine learning ML algorithm. However, since we could not account for previous intensification in the analysis, we cannot conclude whether the signals are indicators of the onset of intensification or of continuing intensification [as was done by Tao et al. (2017)]. As with observational case studies by Zawislak et al. (2016) and Nguyen et al. (2017) and a numerical study by Alvey et al. (2020), future studies should consider the relationship between low- and midlevel thermodynamic distributions with precipitation structure. Future work should also consider how different microphysical distributions are related to TC precipitation distributions as well as linking other observed and derived kinematic fields observed by the TDR (e.g., radial/tangential wind, divergence, vorticity) to the distribution of different precipitation modes. This study can be

expanded upon in the future to include the combined effects of shear and storm motion on the distribution of precipitation modes (e.g., Corbosiero and Molinari 2003), though Wadler et al. (2022) did not find significant differences in thermodynamic distributions using that reference frame and Pei and Jiang (2018) found shear to be the predominant producer of precipitation asymmetries. It would also be beneficial to conduct a numerical modeling study that can assess what physical processes lead to the different distributions of precipitation modes and how the precipitation modes contribute to intensity changes.

5. Conclusions and takeaways

We summarize the major conclusions as follows:

- For all hurricanes, stratiform precipitation is the dominant precipitation mode, within $r^* = 5$ with 82.6% of all observed precipitation. Shallow, moderate, and deep convection constitute 6.6%, 9.5%, and 1.3% of all observed precipitation, respectively.
- The distribution of deep convection is the primary indicator of intensity change. The presence of deep convection favors subsequent intensification when it occurs radially inwards of the RMW and is more symmetrically distributed around the eyewall region, particularly with its presence in the USL quadrant. This confirms the results of previous radar-based studies (Rogers et al. 2013b; Wadler et al. 2018b) that only analyzed the role of deep convection. The identification of deep convection via radar reflectivity is generally downwind of upper-level updrafts. We speculate that deep convection is the primary indicator of intensity change due to heating and humidifying of the entire column of the eyewall, which can lead to surface pressure falls and the subsequent spin up of winds in the boundary layer.
- The distribution of stratiform precipitation does not have a significant relationship to intensity change, which deviates from satellite-based studies. However, those studies have different spatial domains and larger datasets which warrants further investigation in case study comparisons.
- Hurricanes experiencing wind shear with a northerly component resembled precipitation distributions of intensifying storms, while hurricanes experiencing wind shear with a southerly component resembled precipitation distributions of weakening storms. This reflects thermodynamic distributions seen using buoy and dropsonde data in Wadler et al. (2022).

to examine multiple airborne radar datasets in a composite fashion. Our thanks go to Drs. Frank Marks for insightful comments through internal review. We also thank three anonymous reviewers and Editor Dr. Rosimar Rios-Berrios for helping to improve the manuscript. This research was partially supported by the Embry-Riddle Aeronautical University Faculty Research Development Program.

APPENDIX

Calibration of Radar Reflectivity Values

Over the period of this study, different TDR systems were used onboard NOAA's two P3 aircraft (Fischer et al. 2022). The distribution of TDR-derived radar reflectivities can vary from aircraft-to-aircraft (even if the same TC precipitation region is being sampled nearly simultaneously) or from year-to-year. To mitigate observational biases, a bias-correction technique was applied to cases in the TC-RADAR database. To do so, a reference distribution of radar reflectivity was created, using all TDR swath analyses of overwater TCs in the database (Fig. A1). For a given season, we searched for coincident

flights, where the two P3 aircraft [*NOAA42* (*N42*) and *NOAA43* (*N43*)] observed the same TC within 12 h of each other. This temporal constraint is used to identify cases that should have relatively similar distributions of reflectivity, assuming the external forcing on the storms, TC intensity, and the convective structure are not changing significantly over a 12-h period. If at least two coincident flights were identified for both *N42* and *N43*, the observed radar reflectivity distributions for only the coincident flights were compared to the reference reflectivity distribution shown in Fig. A1.

Using a probability matching technique, the distribution of the observed radar reflectivities were shifted to match the reference profile. For example, at a height of 3 km, the 70th percentile of radar reflectivities of the coincident flights for each aircraft were compared to the 70th percentile of radar reflectivities of the reference distribution. Thus, a bias for each aircraft relative to the reference distribution could be identified and then removed by subtracting the reflectivity bias from the observed value at each analysis grid point. This process was repeated for all analysis heights between 0.5 and 10 km. Reflectivity values below the 5th percentile and above the 95th percentile were treated as outliers and bias corrections relative to the 5th and 95th percentiles of the reference profile were applied. For years without sufficient coincident flights, a similar method was applied, but instead of only using coincident flights to identify the reflectivity bias, all TDR analyses from
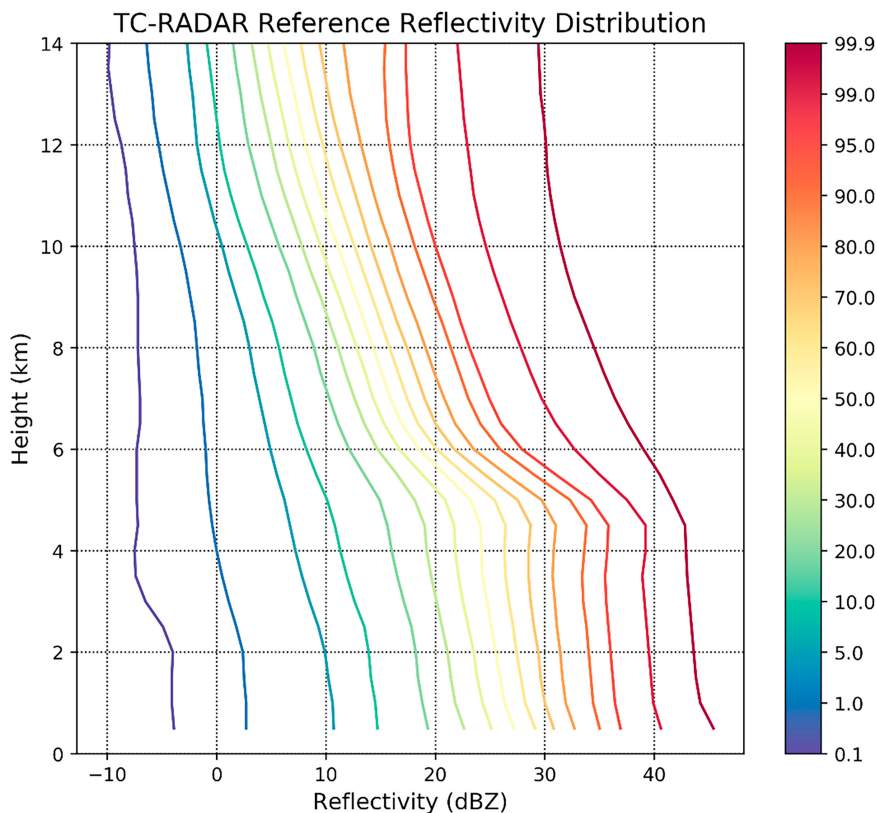

FIG. A1. The vertical distribution of different percentiles of the reference reflectivity (dB*Z*) distribution. Each percentile corresponds to the values shown on the color bar.
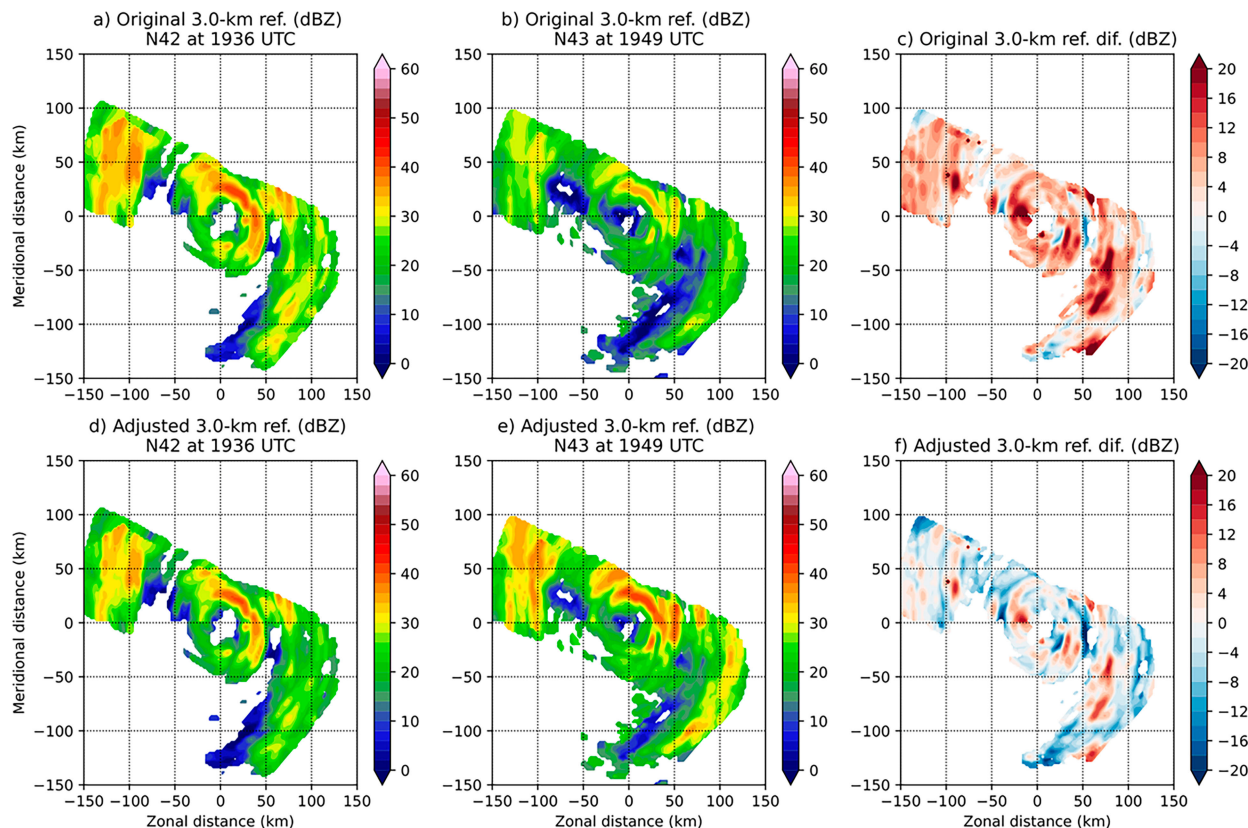
FIG. A2. A comparison of radar reflectivity (shaded; dB*Z*) at 3-km altitude of (a),(b) two swaths into Hurricane Lorenzo at 1900–2000 UTC 29 Sep 2019. The analysis from *N42* in (a) was generated from observations collected approximately 13 min prior to those from *N43* in (b). (c) The difference in the raw radar reflectivities (*N42* − *N43*) are shown. (d),(e) The corresponding bias-corrected reflectivity values for (a) and (b), respectively. (f) The difference in the bias-corrected reflectivities is shown.

the respective aircraft in that year were used to identify reflectivity biases.

An example of the impacts of the reflectivity bias-correction is shown in Fig. A2, for the case of Hurricane Lorenzo (2019). Here, two P3 aircraft sampled the inner core of Lorenzo following a similar flight track, but were offset in time by approximately 13 min. The raw radar TDR reflectivities from each flight (Figs. A2a,b) are associated with relatively large differences, with a pronounced high bias in the analyses from *N42* (Fig. A2c). Once the bias-correction technique was applied (Figs. A2d–f), the TDR analyses from the two aircraft are much more similar, with the pronounced high-bias in the TDR analysis from *N42* removed. Some small differences in the bias-corrected reflectivity pattern remain, presumably due to convective evolution over the 13-min offset in the observing window.

REFERENCES

Alland, J. J., B. H. Tang, and K. L. Corbosiero, 2017: Effects of midlevel dry air on development of the axisymmetric tropical cyclone secondary circulation. *J. Atmos. Sci.*, **74**, 1455–1470, https://doi.org/10.1175/JAS-D-16-0271.1.

——, ——, ——, and G. H. Bryan, 2021a: Synergistic effects of midlevel dry air and vertical wind shear on tropical cyclone

development. Part I: Downdraft ventilation. *J. Atmos. Sci.*, **78**, 763–782, https://doi.org/10.1175/JAS-D-20-0054.1.

——, ——, ——, and ——, 2021b: Combined effects of midlevel dry air and vertical wind shear on tropical cyclone development. Part II: Radial ventilation. *J. Atmos. Sci.*, **78**, 783–796, https://doi.org/10.1175/JAS-D-20-0055.1.

Alvey, G. R., III, J. Zawislak, and E. Zipser, 2015: Precipitation properties observed during tropical cyclone intensity change. *Mon. Wea. Rev.*, **143**, 4476–4492, https://doi.org/10.1175/MWR-D-15-0065.1.

——, E. Zipser, and J. Zawislak, 2020: How does Hurricane Edouard (2014) evolve toward symmetry before rapid intensification? A high-resolution ensemble study. *J. Atmos. Sci.*, **77**, 1329–1351, https://doi.org/10.1175/JAS-D-18-0355.1.

——, M. Fischer, P. Reasor, R. Rogers, and J. Zawislak, 2022: Observed processes underlying the favorable vortex repositioning early in the development of Hurricane Dorian (2019). *Mon. Wea. Rev.*, **150**, 193–213, https://doi.org/10.1175/MWR-D-21-0069.1.

Bell, M. M., and M. T. Montgomery, 2019: Mesoscale processes during the genesis of Hurricane Karl (2010). *J. Atmos. Sci.*, **76**, 2235–2255, https://doi.org/10.1175/JAS-D-18-0161.1.

Bhatia, K. T., and D. S. Nolan, 2013: Relating the skill of tropical cyclone intensity forecasts to the synoptic environment. *Wea. Forecasting*, **28**, 961–980, https://doi.org/10.1175/WAF-D-12-00110.1.

Black, M. L., R. W. Burpee, and F. D. Marks Jr., 1996: Vertical motion characteristics of tropical cyclones determined with airborne Doppler radial velocities. *J. Atmos. Sci.*, **53**, 1887–1909, https://doi.org/10.1175/1520-0469(1996)053<1887:VMCOTC>2.0.CO;2.

——, J. F. Gamache, F. D. Marks Jr., C. E. Samsury, and H. E. Willoughby, 2002: Eastern Pacific Hurricanes Jimena of 1991 and Olivia of 1994: The effect of vertical shear on structure and intensity. *Mon. Wea. Rev.*, **130**, 2291–2312, https://doi.org/10.1175/1520-0493(2002)130<2291:EPHJOA>2.0.CO;2.

Boehm, A. M., and M. M. Bell, 2021: Retrieved thermodynamic structure of Hurricane Rita (2005) from airborne multi–Doppler radar data. *J. Atmos. Sci.*, **78**, 1583–1605, https://doi.org/10.1175/JAS-D-20-0195.1.

Braun, S. A., 2002: A cloud-resolving simulation of Hurricane Bob (1991): Storm structure and eyewall buoyancy. *Mon. Wea. Rev.*, **130**, 1573–1592, https://doi.org/10.1175/1520-0493(2002)130<1573:ACRSOH>2.0.CO;2.

Cangialosi, J. P., E. Blake, M. DeMaria, A. Penny, A. Latto, E. Rappaport, and V. Tallapragada, 2020: Recent progress in tropical cyclone intensity forecasting at the National Hurricane Center. *Wea. Forecasting*, **35**, 1913–1922, https://doi.org/10.1175/WAF-D-20-0059.1.

Chen, B.-F., C. A. Davis, and Y.-H. Kuo, 2018: Effects of low-level flow orientation and vertical shear on the structure and intensity of tropical cyclones. *Mon. Wea. Rev.*, **146**, 2447–2467, https://doi.org/10.1175/MWR-D-17-0379.1.

——, ——, and ——, 2019: An idealized numerical study of shear-relative low-level mean flow on tropical cyclone intensity and size. *J. Atmos. Sci.*, **76**, 2309–2334, https://doi.org/10.1175/JAS-D-18-0315.1.

Chen, H., and D.-L. Zhang, 2013: On the rapid intensification of Hurricane Wilma (2005). Part II: Convective bursts and the upper-level warm core. *J. Atmos. Sci.*, **70**, 146–162, https://doi.org/10.1175/JAS-D-12-062.1.

——, and S. G. Gopalakrishnan, 2015: A study on the asymmetric rapid intensification of Hurricane Earl (2010) using the HWRF system. *J. Atmos. Sci.*, **72**, 531–550, https://doi.org/10.1175/JAS-D-14-0097.1.

Chen, X., J. A. Zhang, and F. D. Marks, 2019: A thermodynamic pathway leading to rapid intensification of tropical cyclones in shear. *Geophys. Res. Lett.*, **46**, 9241–9251, https://doi.org/10.1029/2019GL083667.

——, J.-F. Gu, J. A. Zhang, F. D. Marks, R. F. Rogers, and J. J. Cione, 2021: Boundary layer recovery and precipitation symmetrization preceding rapid intensification of tropical cyclones under shear. *J. Atmos. Sci.*, **78**, 1523–1544, https://doi.org/10.1175/JAS-D-20-0252.1.

Churchill, D. D., and R. A. Houze Jr., 1984: Development and structure of winter monsoon cloud clusters on 10 December 1978. *J. Atmos. Sci.*, **41**, 933–960, https://doi.org/10.1175/1520-0469(1984)041<0933:DASOWM>2.0.CO;2.

Cione, J. J., and E. W. Uhlhorn, 2003: Sea surface temperature variability in hurricanes: Implications with respect to intensity change. *Mon. Wea. Rev.*, **131**, 1783–1796, https://doi.org/10.1175/2562.1.

——, P. G. Black, and S. H. Houston, 2000: Surface observations in the hurricane environment. *Mon. Wea. Rev.*, **128**, 1550–1561, https://doi.org/10.1175/1520-0493(2000)128<1550:SOITHE>2.0.CO;2.

——, E. A. Kalina, J. A. Zhang, and E. W. Uhlhorn, 2013: Observations of air–sea interaction and intensity change in hurricanes.

Mon. Wea. Rev., **141**, 2368–2382, https://doi.org/10.1175/MWR-D-12-00070.1.

Corbosiero, K. L., and J. Molinari, 2003: The relationship between storm motion, vertical wind shear, and convective asymmetries in tropical cyclones. *J. Atmos. Sci.*, **60**, 366–376, https://doi.org/10.1175/1520-0469(2003)060<0366:TRBSMV>2.0.CO;2.

Dai, Y., S. J. Majumdar, and D. S. Nolan, 2021: Tropical cyclone resistance to strong environmental shear. *J. Atmos. Sci.*, **78**, 1275–1293, https://doi.org/10.1175/JAS-D-20-0231.1.

Davis, C. A., and D. A. Ahijevych, 2012: Mesoscale structural evolution of three tropical weather systems observed during PREDICT. *J. Atmos. Sci.*, **69**, 1284–1305, https://doi.org/10.1175/JAS-D-11-0225.1.

DeHart, J. C., R. A. Houze Jr., and R. F. Rogers, 2014: Quadrant distribution of tropical cyclone inner-core kinematics in relation to environmental shear. *J. Atmos. Sci.*, **71**, 2713–2732, https://doi.org/10.1175/JAS-D-13-0298.1.

DeMaria, M., M. Mainelli, L. K. Shay, J. A. Knaff, and J. Kaplan, 2005: Further improvements in the Statistical Hurricane Intensity Prediction Scheme (SHIPS). *Wea. Forecasting*, **20**, 531–543, https://doi.org/10.1175/WAF862.1.

——, C. R. Sampson, J. A. Knaff, and K. D. Musgrave, 2014: Is tropical cyclone intensity guidance improving? *Bull. Amer. Meteor. Soc.*, **95**, 387–398, https://doi.org/10.1175/BAMS-D-12-00240.1.

Didlake, A. C., Jr., and R. A. Houze Jr., 2009: Convective-scale downdrafts in the principal rainband of Hurricane Katrina (2005). *Mon. Wea. Rev.*, **137**, 3269–3293, https://doi.org/10.1175/2009MWR2827.1.

Finocchio, P. M., and S. J. Majumdar, 2017: A statistical perspective on wind profiles and vertical wind shear in tropical cyclone environments of the Northern Hemisphere. *Mon. Wea. Rev.*, **145**, 361–378, https://doi.org/10.1175/MWR-D-16-0221.1.

——, ——, D. S. Nolan, and M. Iskandarani, 2016: Idealized tropical cyclone responses to the height and depth of environmental vertical wind shear. *Mon. Wea. Rev.*, **144**, 2155–2175, https://doi.org/10.1175/MWR-D-15-0320.1.

Fischer, M. S., B. H. Tang, K. L. Corbosiero, and C. M. Rozoff, 2018: Normalized convective characteristics of tropical cyclone rapid intensification events in the North Atlantic and eastern North Pacific. *Mon. Wea. Rev.*, **146**, 1133–1155, https://doi.org/10.1175/MWR-D-17-0239.1.

——, R. F. Rogers, and P. D. Reasor, 2020: The rapid intensification and eyewall replacement cycles of Hurricane Irma (2017). *Mon. Wea. Rev.*, **148**, 981–1004, https://doi.org/10.1175/MWR-D-19-0185.1.

——, P. D. Reasor, R. F. Rogers, and J. F. Gamache, 2022: An analysis of tropical cyclone vortex and convective characteristics in relation to storm intensity using a novel airborne Doppler radar database. *Mon. Wea. Rev.*, **150**, 2255–2278, https://doi.org/10.1175/MWR-D-21-0223.1.

——, ——, B. H. Tang, K. L. Corbosiero, R. D. Torn, and X. Chen, 2023: A tale of two vortex evolutions: Using a high-resolution ensemble to assess the impacts of ventilation on a tropical cyclone rapid intensification event. *Mon. Wea. Rev.*, **151**, 297–320, https://doi.org/10.1175/MWR-D-22-0037.1.

Foerster, A. M., M. M. Bell, P. A. Harr, and S. C. Jones, 2014: Observations of the eyewall structure of Typhoon Sinlaku (2008) during the transformation stage of extratropical transition. *Mon. Wea. Rev.*, **142**, 3372–3392, https://doi.org/10.1175/MWR-D-13-00313.1.

Gamache, J. F., 1997: Evaluation of a fully three-dimensional variational Doppler analysis technique. Preprints, *28th Conf. on Radar Meteorology,* Austin, TX, Amer. Meteor. Soc., 422–423.

Gu, J.-F., Z.-M. Tan, and X. Qiu, 2019: Intensification variability of tropical cyclones in directional shear flows: Vortex tilt–convection coupling. *J. Atmos. Sci.*, **76**, 1827–1844, https://doi.org/10.1175/JAS-D-18-0282.1.

Harnos, D. S., and S. W. Nesbitt, 2016a: Varied pathways for simulated tropical cyclone rapid intensification. Part I: Precipitation and environment. *Quart. J. Roy. Meteor. Soc.*, **142**, 1816–1831, https://doi.org/10.1002/qj.2780.

——, and ——, 2016b: Varied pathways for simulated tropical cyclone rapid intensification. Part II: Vertical motion and cloud populations. *Quart. J. Roy. Meteor. Soc.*, **142**, 1832–1846, https://doi.org/10.1002/qj.2778.

Hazelton, A. T., and R. E. Hart, 2013: Hurricane eyewall slope as determined from airborne radar reflectivity data: Composites and case studies. *Wea. Forecasting*, **28**, 368–386, https://doi.org/10.1175/WAF-D-12-00037.1.

——, G. J. Alaka Jr., L. Cowan, M. Fischer, and S. Gopalakrishnan, 2021: Understanding the processes causing the early intensification of Hurricane Dorian through an ensemble of the Hurricane Analysis and Forecast System (HAFS). *Atmosphere*, **12**, 93, https://doi.org/10.3390/atmos12010093.

Hence, D. A., and R. A. Houze Jr., 2008: Kinematic structure of convective-scale elements in the rainbands of Hurricanes Katrina and Rita (2005). *J. Geophys. Res.*, **113**, D15108, https://doi.org/10.1029/2007JD009429.

Houze, R. A., Jr., F. D. Marks Jr., and R. A. Black, 1992: Dual-aircraft investigation of the inner core of Hurricane Norbert. Part II: Mesoscale distribution of ice particles. *J. Atmos. Sci.*, **49**, 943–963, https://doi.org/10.1175/1520-0469(1992)049<0943:DAIOTI>2.0.CO;2.

Jaimes de la Cruz, B., L. K. Shay, J. B. Wadler, and J. E. Rudzin, 2021: On the hyperbolicity of the bulk air–sea heat flux functions: Insights into the efficiency of air–sea moisture disequilibrium for tropical cyclone intensification. *Mon. Wea. Rev.*, **149**, 1517–1534, https://doi.org/10.1175/MWR-D-20-0324.1.

Jiang, H., 2012: The relationship between tropical cyclone intensity change and the strength of inner-core convection. *Mon. Wea. Rev.*, **140**, 1164–1176, https://doi.org/10.1175/MWR-D-11-00134.1.

——, J. P. Zagrodnik, C. Tao, and E. J. Zipser, 2018: Classifying precipitation types in tropical cyclones using the NRL 37 GHz color product. *J. Geophys. Res. Atmos.*, **123**, 5509–5524, https://doi.org/10.1029/2018JD028324.

Jones, S. C., 1995: The evolution of vortices in vertical shear: Initially barotropic vortices. *Quart. J. Roy. Meteor. Soc.*, **121**, 821–851, https://doi.org/10.1002/qj.49712152406.

Jorgensen, D. F., 1984: Mesoscale and convective-scale characteristics of mature hurricanes. Part I: General observations by research aircraft. *J. Atmos. Sci.*, **41**, 1268–1286, https://doi.org/10.1175/1520-0469(1984)041<1268:MACSCO>2.0.CO;2.

——, E. J. Zipser, and M. A. LeMone, 1985: Vertical motions in intense hurricanes. *J. Atmos. Sci.*, **42**, 839–856, https://doi.org/10.1175/1520-0469(1985)042<0839:VMIIH>2.0.CO;2.

Kieper, M., and H. Jiang, 2012: Predicting tropical cyclone rapid intensification using the 37 GHz ring pattern identified from passive microwave measurements. *Geophys. Res. Lett.*, **39**, L13804, https://doi.org/10.1029/2012GL052115.

Klotzbach, P. J., S. G. Bowen, R. Pielke Jr., and M. Bell, 2018: Continental U.S. hurricane landfall frequency and associated damage: Observations and future risks. *Bull. Amer. Meteor. Soc.*, **99**, 1359–1376, https://doi.org/10.1175/BAMS-D-17-0184.1.

Leighton, H., S. Gopalakrishnan, J. A. Zhang, R. F. Rogers, Z. Zhang, and V. Tallapragada, 2018: Azimuthal distribution of deep convection, environmental factors, and tropical cyclone rapid intensification: A perspective from HWRF ensemble forecasts of Hurricane Edouard (2014). *J. Atmos. Sci.*, **75**, 275–295, https://doi.org/10.1175/JAS-D-17-0171.1.

Marks, F. D., Jr., and R. A. Houze Jr., 1987: Inner core structure of Hurricane Alicia from airborne Doppler radar observations. *J. Atmos. Sci.*, **44**, 1296–1317, https://doi.org/10.1175/1520-0469(1987)044<1296:ICSOHA>2.0.CO;2.

——, and L. K. Shay, 1998: Landfalling tropical cyclones: Forecast problems and associated research opportunities. *Bull. Amer. Meteor. Soc.*, **79**, 305–323, https://doi.org/10.1175/1520-0477(1998)079<0305:LTCFPA>2.0.CO;2.

Massey, F. J., Jr., 1951: The Kolmogorov-Smirnov test for goodness of fit. *J. Amer. Stat. Assoc.*, **46**, 68–78, https://doi.org/10.1080/01621459.1951.10500769.

Molinari, J., and D. Vollaro, 2010: Rapid intensification of a sheared tropical storm. *Mon. Wea. Rev.*, **138**, 3869–3885, https://doi.org/10.1175/2010MWR3378.1.

——, ——, and K. L. Corbosiero, 2004: Tropical cyclone formation in a sheared environment: A case study. *J. Atmos. Sci.*, **61**, 2493–2509, https://doi.org/10.1175/JAS3291.1.

——, P. Dodge, D. Vollaro, K. L. Corbosiero, and F. Marks, Jr., 2006: Mesoscale aspects of the downshear reformation of a tropical cyclone. *J. Atmos. Sci.*, **63**, 341–354, https://doi.org/10.1175/JAS3591.1.

——, J. Frank, and D. Vollaro, 2013: Convective bursts, downdraft cooling, and boundary layer recovery in a sheared tropical storm. *Mon. Wea. Rev.*, **141**, 1048–1060, https://doi.org/10.1175/MWR-D-12-00135.1.

Montgomery, M. T., L. L. Lussier III, R. W. Moore, and Z. Wang, 2010: The genesis of Typhoon Nuri as observed during the Tropical Cyclone Structure 2008 (TCS-08) field experiment—Part 1: The role of the easterly wave critical layer. *Atmos. Chem. Phys.*, **10**, 9879–9900, https://doi.org/10.5194/acp-10-9879-2010.

Munsell, E. B., F. Zhang, J. A. Sippel, S. A. Braun, and Y. Weng, 2017: Dynamics and predictability of the intensification of Hurricane Edouard (2014). *J. Atmos. Sci.*, **74**, 573–595, https://doi.org/10.1175/JAS-D-16-0018.1.

Nam, C. C., and M. M. Bell, 2021: Multiscale shear impacts during the genesis of Hagupit (2008). *Mon. Wea. Rev.*, **149**, 551–569, https://doi.org/10.1175/MWR-D-20-0133.1.

Nguyen, L. T., R. F. Rogers, and P. D. Reasor, 2017: Thermodynamic and kinematic influences on precipitation symmetry in sheared tropical cyclones: Bertha and Cristobal (2014). *Mon. Wea. Rev.*, **145**, 4423–4446, https://doi.org/10.1175/MWR-D-17-0073.1.

——, ——, J. Zawislak, and J. A. Zhang, 2019: Assessing the influence of convective downdrafts and surface enthalpy fluxes on tropical cyclone intensity change in moderate vertical wind shear. *Mon. Wea. Rev.*, **147**, 3519–3534, https://doi.org/10.1175/MWR-D-18-0461.1.

Nolan, D. S., and L. D. Grasso, 2003: Nonhydrostatic, three-dimensional perturbations to balanced, hurricane-like vortices. Part II: Symmetric response and nonlinear simulations. *J. Atmos. Sci.*, **60**, 2717–2745, https://doi.org/10.1175/1520-0469(2003)060<2717:NTPTBH>2.0.CO;2.

——, and M. G. McGauley, 2012: Tropical cyclogenesis in wind shear: Climatological relationships and physical processes.

Cyclones: Formation, Triggers, and Control, K. Oouchi and H. Fudeyasu, Eds., Nova Science Publishers, 1–36.

——, Y. Moon, and D. P. Stern, 2007: Tropical cyclone intensification from asymmetric convection: Energetics and efficiency. *J. Atmos. Sci.*, **64**, 3377–3405, https://doi.org/10.1175/JAS3988.1.

Onderlinde, M. J., and D. S. Nolan, 2014: Environmental helicity and its effects on development and intensification of tropical cyclones. *J. Atmos. Sci.*, **71**, 4308–4320, https://doi.org/10.1175/JAS-D-14-0085.1.

——, and ——, 2016: Tropical cyclone–relative environmental helicity and the pathways to intensification in shear. *J. Atmos. Sci.*, **73**, 869–890, https://doi.org/10.1175/JAS-D-15-0261.1.

Pei, Y., and H. Jiang, 2018: Quantification of precipitation asymmetries of tropical cyclones using 16-yr TRMM observations. *J. Geophys. Res. Atmos.*, **123**, 8091–8114, https://doi.org/10.1029/2018JD028545.

Pendergrass, A. G., and H. E. Willoughby, 2009: Diabatically induced secondary flows in tropical cyclones. Part I: Quasi-steady forcing. *Mon. Wea. Rev.*, **137**, 805–821, https://doi.org/10.1175/2008MWR2657.1.

Pielke, R. A., Jr., and C. W. Landsea, 1998: Normalized hurricane damages in the United States: 1925–95. *Wea. Forecasting*, **13**, 621–631, https://doi.org/10.1175/1520-0434(1998)013<0621:NHDITU>2.0.CO;2.

——, J. Gratz, C. W. Landsea, D. Collins, M. A. Saunders, and R. Muslin, 2008: Normalized hurricane damage in the United States: 1900–2005. *Nat. Hazards Rev.*, **9**, 29–42, https://doi.org/10.1061/(ASCE)1527-6988(2008)9:1(29).

Rappin, E. D., and D. S. Nolan, 2012: The effect of vertical shear orientation on tropical cyclogenesis. *Quart. J. Roy. Meteor. Soc.*, **138**, 1035–1054, https://doi.org/10.1002/qj.977.

Reasor, P. D., and M. D. Eastin, 2012: Rapidly intensifying Hurricane Guillermo (1997). Part II: Resilience in shear. *Mon. Wea. Rev.*, **140**, 425–444, https://doi.org/10.1175/MWR-D-11-00080.1.

——, ——, and J. F. Gamache, 2009: Rapidly intensifying Hurricane Guillermo (1997). Part I: Low-wavenumber structure and evolution. *Mon. Wea. Rev.*, **137**, 603–631, https://doi.org/10.1175/2008MWR2487.1.

——, R. Rogers, and S. Lorsolo, 2013: Environmental flow impacts on tropical cyclone structure diagnosed from airborne Doppler radar composites. *Mon. Wea. Rev.*, **141**, 2949–2969, https://doi.org/10.1175/MWR-D-12-00334.1.

Reynolds, R. W., and D. C. Marsico, 1993: An improved real-time global sea surface temperature analysis. *J. Climate*, **6**, 114–119, https://doi.org/10.1175/1520-0442(1993)006<0114:AIRTGS>2.0.CO;2.

Riemer, M., 2016: Meso-β-scale environment for the stationary band complex of vertically sheared tropical cyclones. *Quart. J. Roy. Meteor. Soc.*, **142**, 2442–2451, https://doi.org/10.1002/qj.2837.

——, M. T. Montgomery, and M. E. Nicholls, 2010: A new paradigm for intensity modification of tropical cyclones: Thermodynamic impact of vertical wind shear on the inflow layer. *Atmos. Chem. Phys.*, **10**, 3163–3188, https://doi.org/10.5194/acp-10-3163-2010.

——, ——, and ——, 2013: Further examination of the thermodynamic modification of the inflow layer of tropical cyclones by vertical wind shear. *Atmos. Chem. Phys.*, **13**, 327–346, https://doi.org/10.5194/acp-13-327-2013.

Rios-Berrios, R., and R. D. Torn, 2017: Climatological analysis of tropical cyclone intensity changes under moderate vertical

wind shear. *Mon. Wea. Rev.*, **145**, 1717–1738, https://doi.org/10.1175/MWR-D-16-0350.1.

——, ——, and C. A. Davis, 2016a: An ensemble approach to investigate tropical cyclone intensification in sheared environments. Part I: Katia (2011). *J. Atmos. Sci.*, **73**, 71–93, https://doi.org/10.1175/JAS-D-15-0052.1.

——, ——, and ——, 2016b: An ensemble approach to investigate tropical cyclone intensification in sheared environments. Part II: Ophelia (2011). *J. Atmos. Sci.*, **73**, 1555–1575, https://doi.org/10.1175/JAS-D-15-0245.1.

——, C. A. Davis, and R. D. Torn, 2018: A hypothesis for the intensification of tropical cyclones under moderate vertical wind shear. *J. Atmos. Sci.*, **75**, 4149–4173, https://doi.org/10.1175/JAS-D-18-0070.1.

Rogers, R. F., 2010: Convective-scale structure and evolution during a high-resolution simulation of tropical cyclone rapid intensification. *J. Atmos. Sci.*, **67**, 44–70, https://doi.org/10.1175/2009JAS3122.1.

——, and Coauthors, 2006: The intensity forecasting experiment: A NOAA multiyear field program for improving tropical cyclone intensity forecasts. *Bull. Amer. Meteor. Soc.*, **87**, 1523–1538, https://doi.org/10.1175/BAMS-87-11-1523.

——, F. Marks Jr., and T. Marchok, 2009: Tropical cyclone rainfall. *Encyclopedia of Hydrological Sciences*, M. G. Anderson and J. J. McDonnell, Eds., John Wiley and Sons, https://doi.org/10.1002/0470848944.hsa030.

——, S. Lorsolo, P. Reasor, J. Gamache, and F. Marks, 2012: Multiscale analysis of tropical cyclone kinematic structure from airborne Doppler radar composites. *Mon. Wea. Rev.*, **140**, 77–99, https://doi.org/10.1175/MWR-D-10-05075.1.

——, and Coauthors, 2013a: NOAA's hurricane intensity forecasting experiment: A progress report. *Bull. Amer. Meteor. Soc.*, **94**, 859–882, https://doi.org/10.1175/BAMS-D-12-00089.1.

——, P. Reasor, and S. Lorsolo, 2013b: Airborne Doppler observations of the inner-core structural differences between intensifying and steady-state tropical cyclones. *Mon. Wea. Rev.*, **141**, 2970–2991, https://doi.org/10.1175/MWR-D-12-00357.1.

——, P. D. Reasor, and J. A. Zhang, 2015: Multiscale structure and evolution of Hurricane Earl (2010) during rapid intensification. *Mon. Wea. Rev.*, **143**, 536–562, https://doi.org/10.1175/MWR-D-14-00175.1.

——, J. A. Zhang, J. Zawislak, H. Jiang, G. R. Alvey III, E. J. Zipser, and S. N. Stevenson, 2016: Observations of the structure and evolution of Hurricane Edouard (2014) during intensity change. Part II: Kinematic structure and the distribution of deep convection. *Mon. Wea. Rev.*, **144**, 3355–3376, https://doi.org/10.1175/MWR-D-16-0017.1.

——, P. D. Reasor, J. A. Zawislak, and L. T. Nguyen, 2020: Precipitation processes and vortex alignment during the intensification of a weak tropical cyclone in moderate vertical shear. *Mon. Wea. Rev.*, **148**, 1899–1929, https://doi.org/10.1175/MWR-D-19-0315.1.

Rudzin, J. E., S. Chen, E. R. Sanabia, and S. R. Jayne, 2020: The air-sea response during Hurricane Irma's (2017) rapid intensification over the Amazon-Orinoco River plume as measured by atmospheric and oceanic observations. *J. Geophys. Res. Atmos.*, **125**, e2019JD032368, https://doi.org/10.1029/2019JD032368.

Ryglicki, D. R., C. S. Velden, P. D. Reasor, D. Hodyss, and J. D. Doyle, 2021: Observations of atypical rapid intensification characteristics in Hurricane Dorian (2019). *Mon. Wea. Rev.*, **149**, 2131–2150, https://doi.org/10.1175/MWR-D-20-0413.1.

Schecter, D. A., 2022: Intensification of tilted tropical cyclones over relatively cool and warm oceans in idealized numerical

simulations. *J. Atmos. Sci.*, **79**, 485–512, https://doi.org/10.1175/JAS-D-21-0051.1.

Shi, D., and G. Chen, 2021: The implication of outflow structure for the rapid intensification of tropical cyclones under vertical wind shear. *Mon. Wea. Rev.*, **149**, 4107–4127, https://doi.org/10.1175/MWR-D-21-0141.1.

Smith, R. K., and M. T. Montgomery, 2016: The efficiency of diabatic heating and tropical cyclone intensification. *Quart. J. Roy. Meteor. Soc.*, **142**, 2081–2086, https://doi.org/10.1002/qj.2804.

Steiner, M., R. A. Houze Jr., and S. E. Yuter, 1995: Climatological characterization of three-dimensional storm structure from operational radar and rain gauge data. *J. Appl. Meteor.*, **34**, 1978–2007, https://doi.org/10.1175/1520-0450(1995)034<1978:CCOTDS>2.0.CO;2.

Stevenson, S. N., K. L. Corbosiero, and J. Molinari, 2014: The convective evolution and rapid intensification of Hurricane Earl (2010). *Mon. Wea. Rev.*, **142**, 4364–4380, https://doi.org/10.1175/MWR-D-14-00078.1.

——, ——, M. DeMaria, and J. L. Vigh, 2018: A 10-year survey of tropical cyclone inner-core lightning bursts and their relationship to intensity change. *Wea. Forecasting*, **33**, 23–36, https://doi.org/10.1175/WAF-D-17-0096.1.

Stone, Ž., G. R. Alvey III, J. P. Dunion, M. S. Fischer, D. J. Raymond, R. F. Rogers, S. Sentić, and J. Zawislak, 2023: Thermodynamic contribution to vortex alignment and rapid intensification of Hurricane Sally (2020). *Mon. Wea. Rev.*, **151**, 931–951, https://doi.org/10.1175/MWR-D-22-0201.1.

Tang, B., and K. Emanuel, 2010: Midlevel ventilation's constraint on tropical cyclone intensity. *J. Atmos. Sci.*, **67**, 1817–1830, https://doi.org/10.1175/2010JAS3318.1.

——, and ——, 2012: Sensitivity of tropical cyclone intensity to ventilation in an axisymmetric model. *J. Atmos. Sci.*, **69**, 2394–2413, https://doi.org/10.1175/JAS-D-11-0232.1.

Tao, C., and H. Jiang, 2015: Distributions of shallow to very deep precipitation–convection in rapidly intensifying tropical cyclones. *J. Climate*, **28**, 8791–8824, https://doi.org/10.1175/JCLI-D-14-00448.1.

——, ——, and J. Zawislak, 2017: The relative importance of stratiform and convective rainfall in rapidly intensifying tropical cyclones. *Mon. Wea. Rev.*, **145**, 795–809, https://doi.org/10.1175/MWR-D-16-0316.1.

Tuleya, R. E., and Y. Kurihara, 1981: A numerical study on the effects of environmental flow on tropical storm genesis. *Mon. Wea. Rev.*, **109**, 2487–2506, https://doi.org/10.1175/1520-0493(1981)109<2487:ANSOTE>2.0.CO;2.

Vigh, J. L., and W. H. Schubert, 2009: Rapid development of the tropical cyclone warm core. *J. Atmos. Sci.*, **66**, 3335–3350, https://doi.org/10.1175/2009JAS3092.1.

Wadler, J. B., J. A. Zhang, B. Jaimes, and L. K. Shay, 2018a: Downdrafts and the evolution of boundary layer thermodynamics in Hurricane Earl (2010) before and during rapid intensification. *Mon. Wea. Rev.*, **146**, 3545–3565, https://doi.org/10.1175/MWR-D-18-0090.1.

——, R. F. Rogers, and P. D. Reasor, 2018b: The relationship between spatial variations in the structure of convective bursts and tropical cyclone intensification as determined by airborne Doppler radar. *Mon. Wea. Rev.*, **146**, 761–780, https://doi.org/10.1175/MWR-D-17-0213.1.

——, D. S. Nolan, J. A. Zhang, and L. K. Shay, 2021a: The thermodynamic characteristics of downdrafts in tropical cyclones

using idealized simulations of different intensities. *J. Atmos. Sci.*, **78**, 3503–3524, https://doi.org/10.1175/JAS-D-21-0006.1.

——, J. A. Zhang, R. F. Rogers, B. Jaimes, and L. K. Shay, 2021b: The rapid intensification of Hurricane Michael (2018): Storm structure and the relationship to environmental and air–sea interactions. *Mon. Wea. Rev.*, **149**, 245–267, https://doi.org/10.1175/MWR-D-20-0145.1.

——, J. J. Cione, J. A. Zhang, E. Kalina, and J. Kaplan, 2022: The effects of environmental wind shear direction on tropical cyclone boundary layer thermodynamics and intensity change from multiple observational datasets. *Mon. Wea. Rev.*, **150**, 115–134, https://doi.org/10.1175/MWR-D-21-0022.1.

Yu, C.-L., B. Tang, and R. G. Fovell, 2023: Tropical cyclone tilt and precession in moderate shear: Precession hiatus in a critical shear regime. *J. Atmos. Sci.*, **80**, 909–932, https://doi.org/10.1175/JAS-D-22-0200.1.

Yuter, S. E., and R. A. Houze Jr., 1995: Three-dimensional kinematic and microphysical evolution of Florida cumulonimbus. Part II: Frequency distributions of vertical velocity, reflectivity, and differential reflectivity. *Mon. Wea. Rev.*, **123**, 1941–1963, https://doi.org/10.1175/1520-0493(1995)123<1941:TDKAME>2.0.CO;2.

——, and ——, 1997: Measurements of raindrop size distributions over the Pacific warm pool and implications for *Z–R* relations. *J. Appl. Meteor.*, **36**, 847–867, https://doi.org/10.1175/1520-0450(1997)036<0847:MORSDO>2.0.CO;2.

Zagrodnik, J. P., and H. Jiang, 2014: Rainfall, convection, and latent heating distributions in rapidly intensifying tropical cyclones. *J. Atmos. Sci.*, **71**, 2789–2809, https://doi.org/10.1175/JAS-D-13-0314.1.

Zawislak, J., H. Jiang, G. R. Alvey III, E. J. Zipser, R. F. Rogers, J. A. Zhang, and S. N. Stevenson, 2016: Observations of the structure and evolution of Hurricane Edouard (2014) during intensity change. Part I: Relationship between the thermodynamic structure and precipitation. *Mon. Wea. Rev.*, **144**, 3333–3354, https://doi.org/10.1175/MWR-D-16-0018.1.

——, and Coauthors, 2022: Accomplishments of NOAA's airborne hurricane field program and a broader future approach to forecast improvement. *Bull. Amer. Meteor. Soc.*, **103**, E311–E338, https://doi.org/10.1175/BAMS-D-20-0174.1.

Zhang, D.-L., and H. Chen, 2012: Importance of the upper-level warm core in the rapid intensification of a tropical cyclone. *Geophys. Res. Lett.*, **39**, L02806, https://doi.org/10.1029/2011GL050578.

Zhang, J. A., and R. F. Rogers, 2019: Effects of parameterized boundary layer structure on hurricane rapid intensification in shear. *Mon. Wea. Rev.*, **147**, 853–871, https://doi.org/10.1175/MWR-D-18-0010.1.

——, ——, P. D. Reasor, E. W. Uhlhorn, and F. D. Marks Jr., 2013: Asymmetric hurricane boundary layer structure from dropsonde composites in relation to the environmental vertical wind shear. *Mon. Wea. Rev.*, **141**, 3968–3984, https://doi.org/10.1175/MWR-D-12-00335.1.

——, J. J. Cione, E. A. Kalina, E. W. Uhlhorn, T. Hock, and J. A. Smith, 2017: Observations of infrared sea surface temperature and air–sea interaction in Hurricane Edouard (2014) using GPS dropsondes. *J. Atmos. Oceanic Technol.*, **34**, 1333–1349, https://doi.org/10.1175/JTECH-D-16-0211.1.

——, R. F. Rogers, P. D. Reasor, and J. Gamache, 2023: The mean kinematic structure of the tropical cyclone boundary layer and its relationship to intensity change. *Mon. Wea. Rev.*, **151**, 63–84, https://doi.org/10.1175/MWR-D-21-0335.1.